Department of Physics and Astronomy
University of Heidelberg

Diploma thesis

in Physics

submitted by

Martin Gerhard Ries

born in Gießen

2010

A magneto-optical trap for the preparation of a three-component Fermi gas in an optical lattice

This diploma thesis has been carried out by Martin Gerhard Ries

at the

Physikalisches Institut Heidelberg

and the

Max-Planck-Institute for Nuclear Physics

under the supervision of

Professor Selim Jochim

Abstract

This thesis reports on the first steps towards the preparation of an ultracold three-component Fermi gas of ^{6}Li in an optical lattice.

A vacuum chamber and a magneto-optical trap (MOT) for ^{6}Li were set up and characterized. The MOT will serve as a first trapping and cooling stage, from which atoms can be loaded into an optical dipole trap for further cooling. The crucial parameters of the apparatus are a high MOT loading rate for fast experiment cycles, and a low background pressure, which will provide an undisturbed environment and thus a long lifetime for atoms in the lattice.

The loading rate of the MOT was measured to be $L \approx 3 \cdot 10^8$ atoms/s at an oven temperature of $T_{oven} = 350°$C, which exceeds current state of the art experiments and will allow for loading times of less than one second in the planned experiments. The background collision limited lifetime of atoms in the MOT is $\tau \approx 23$ min. Collisions with the background gas are therefore not expected to be a limiting factor for the lifetime of atoms in the optical lattice.

Zusammenfassung

Diese Arbeit behandelt die ersten Schritte zur Herstellung eines ultrakalten, dreikomponentigen Fermigases aus ^{6}Li Atomen in einem optischen Gitter.

Im Verlauf der Arbeit wurden eine Vakuumkammer und eine magneto-optische Falle (MOT) für ^{6}Li aufgebaut und charakterisiert. Die MOT wird eingesetzt werden um Atome einzufangen und vorzukühlen, bevor sie zur weiteren Kühlung in eine optische Dipolfalle transferiert werden. Die wichtigsten Eigenschaften des Apparates sind hohe Laderaten, welche schnelle Experimentzyklen ermöglichen werden, und ein niedriger Druck in der Experimentierkammer. Dieser führt zu einer kleinen Stoßrate der gefangenen Atome mit dem Hintergrundgas, und wird somit eine lange Lebensdauer der Atome im Gitter ermöglichen.

Die Laderate der MOT bei einer Ofentemperatur von $T_{oven} = 350°$C wurde als $L \approx 3 \cdot 10^8$ Atome/s gemessen. Diese Laderate übertrifft die aktueller ^{6}Li Experimente. Sie erlaubt es, eine für die geplanten Experimente ausreichende Menge Atome innerhalb von weniger als einer Sekunde einzufangen. Die durch Stöße mit dem Hintergrundgas bestimmte Lebensdauer von Atomen in der MOT ist $\tau \approx 23$ min. Wir erwarten daher, dass diese Stöße die Lebensdauer von Atomen im optischen Gitter nicht limitieren werden.

Contents

viii

Chapter 1

Introduction

Soon after the discovery of the spin degree of freedom in the early 20th century, its fundamental influence on the behavior of particles was discovered. All particles can be classified into two categories: integer spin particles, which are called bosons after Satyendranath Bose and half integer spin particles, which are called fermions after Enrico Fermi.

Among the elementary particles, all mediators of fundamental forces are bosons. An example is the photon, which mediates the electromagnetic interaction. All constituents of matter, on the other hand, are fermionic. The most prominent example is the electron, which has a spin of 1/2.

Bosons follow the Bose-Einstein statistics, where the wave function is symmetric against particle exchange. Fermions on the other hand follow the Fermi-Dirac statistics and have an antisymmetric wave function. This leads to an important consequence: whereas two or more identical bosons can occupy the same quantum state, identical fermions cannot. Their behavior is governed by the Pauli exclusion principle.

Not only elementary particles, but also compound particles such as nuclei or atoms can be classified as bosons or fermions, according to their total spin. During the last years, it has become experimentally feasible to prepare dilute gases of atoms in a regime where their quantum statistical behavior can be observed. This is achieved by cooling a trapped atomic cloud to ultra low temperatures and thus increasing its phase space density until the wave functions of the atoms start to overlap.

One great advantage of these ultracold atom ensembles is that it is possible to tune their properties. For instance, the trap geometry and depth can be adjusted by changing parameters of the trapping lasers or magnetic fields. In addition, the interaction strength between the atoms can be controlled with the help of Feshbach resonances. The atoms can thus serve as a clean and controllable model for various quantum systems.

One important milestone in the history of research on ultracold quantum gases was the first observation of Bose-Einstein condensation (BEC) in 1995 [And95, Dav95]. Until the first quantum degenerate Fermi gas was obtained in 1999 [DeM99], an additional experimental challenge had to be overcome. Due to their antisymmetric wave function, identical fermions do not scatter with each other at low temperatures, where only s-wave scattering is possible. Thermalization through elastic scattering is a crucial prerequisite for evaporative cooling, which therefore requires two distinguishable kinds of particles.

These two components can either be realized by a mixture of two different atomic species, or by two spin states of the same species. One realization of the latter approach is provided by the two lowest Zeeman substates of ^{6}Li. In 2002, the first quantum degenerate ^{6}Li gas in an all optical trap was achieved [Gra02]. The optical approach allowed for the application of homogeneous magnetic fields, which can be used to control the interaction strength between the atoms via Feshbach resonances.

This technology made it possible to create diatomic molecules on the one side of the Feshbach resonance, where the interatomic potential supports a bound state [Str03, Joc03a]. As they consist of two fermions, the molecules are bosonic. In 2003, the Bose-Einstein condensation of molecules could thus be observed [Joc03b, Gre03, Zwi03]. Hence, this side of the resonance was called the BEC side.

At the other side of the resonance, the system consists of fermions with an attractive interaction, as proposed in Bardeen, Cooper and Schrieffer's theory of superfluidity [Bar57]. The atom ensemble, which shows superfluid properties [Zwi05], can thus be used as a model system for superconductivity, which is a manifestation of superfluidity in the electron gas. The two hyperfine states of the atoms represent the two spin orientations ($\uparrow$, $\downarrow$) of the electrons.

By adiabatically sweeping the system over the Feshbach resonance, the superfluid pairs of fermions can be continuously merged into bosonic molecules, which then condense into the ground state. This phenomenon is known as the BCS-BEC crossover.

In order to simulate electrons in the periodic potential of a solid-state, two-component Fermi gases can be loaded into optical lattices [Ess10]. By tuning the lattice depth and spacing as well as the interaction strength of the atoms, the system can be adapted to various applications. One important goal of this research is to study d-wave superfluidity, which is believed to be the mechanism responsible for high-T_c superconductivity.

The properties of the system change fundamentally as soon as a third component is added to the Fermi gas. This way, a system with tunable interactions and an approximate SU(3) symmetry can be created. Such systems can be related to high-energy physics such as color superfluidity or baryon formation in quark matter [Rap07, Wil07].

The first experiments with a three-component Fermi gas consisting of the three lowest Zeeman substates of ^{6}Li were performed in our group in 2008 [Ott08]. It turned out that the behavior of this system is dominated by inelastic three-body collisions as soon as interactions are tuned to large values. In these collisions, three atoms become bound in a so-called Efimov trimer and are lost from the trap.

While the Efimov effect is interesting in itself, the inelastic collisions unfortunately limit the studies of many-body physics in the system. This limitation can be overcome by loading the three-component gas into an optical lattice. If the three-body decay rate is much higher than the tunneling rate between the sites of the lattice, tunneling is predicted to be suppressed by the quantum Zeno effect [Kan09]. Hence, the system should be stabilized and studies of its many-body physics should be possible.

In the course of this thesis, the construction of an apparatus for the creation of a three-component Fermi gas in an optical lattice was started. A vacuum chamber was constructed and a magneto-optical trap (MOT) for ^{6}Li was set up and characterized. It will serve as a first trapping and cooling stage on the way to an intriguing system.

Outline

This diploma thesis begins with a short review of the theory of ultracold Fermi gases in chapter 2, focussing on scattering interactions between the atoms and their tunability with the help of Feshbach resonances. In addition, the BEC-BCS crossover and the concept of universality are introduced.

After reviewing aspects of fundamental atom-light interactions, chapter 3 describes the laser trapping and cooling techniques used in our setup. The Zeeman slower and the MOT, which have already been set up, are discussed in detail. Although they have yet to be set up, dipole traps and optical lattices are also reviewed.

Chapter 4 describes the apparatus which was built during this thesis. The vacuum chamber and the laser system are reviewed separately before the parameters of the trapping setup are discussed. At the end of the chapter, the experiment control system and the imaging system are briefly introduced.

A characterization of our MOT is provided in chapter 5. The loading rate was measured to be $3 \cdot 10^8$ atoms/s at a moderate oven temperature of 350°C. Short experiment cycles and a long oven lifetime will therefore be possible. The lifetime of atoms in the MOT was measured to be approximately 23 minutes. This indicates a low background pressure in the main chamber, which is crucial for future experiments in shallow dipole traps.

In chapter 6, the results of this work are summarized and an outlook over the planned next steps is provided.

Chapter 2

Ultracold Fermi Gases

Ultracold Fermi gases can serve as versatile model systems for various physical phenomena. This is mainly due to the intriguing possibility of tuning their interaction strength to almost arbitrary values by means of Feshbach resonances. For diverging interaction strength, an ultracold Fermi gas can enter the universal regime, where all properties of the gas are determined only by the scattering length a. This way, it can serve as a model for other universal Fermi systems such as for example neutron stars.

This chapter explains some of the most important properties of ultracold Fermi gases. Starting with a non-interacting Fermi gas in a harmonic trap, interactions are added to the system in the form of scattering between the particles. After a review of scattering resonances and Feshbach resonances, universality and the BEC-BCS crossover will be introduced. The chapter will conclude with some details about the ^{6}Li system which we will use for our experiments.

2.1 Ideal Fermi gas

Unlike in Bose gases, where all particles condense into the ground state of the system for $T \to 0$ [Ein25], the particles in a Fermi gas are subject to the Pauli exclusion principle. They will therefore follow the Fermi-Dirac distribution:

$$f(\mathbf{r}, \mathbf{p}) = \frac{1}{e^{\left(\frac{\mathbf{p}^2}{2m} + V(\mathbf{r}) - \mu\right)/k_B T} + 1} \tag{2.1}$$

with the external trapping potential $V(\mathbf{r})$, the chemical potential μ, and the Boltzmann constant k_B. For $T = 0$, the distribution simplifies to

$$f(\mathbf{r}, \mathbf{p}) = \begin{cases} 1 & ; \ \frac{\mathbf{p}^2}{2m} + V(\mathbf{r}) < \mu \\ 0 & ; \ \frac{\mathbf{p}^2}{2m} + V(\mathbf{r}) > \mu \ . \end{cases} \tag{2.2}$$

5

This means that for $T = 0$, the energy states of a trap are populated continuously from the lowest state to the chemical potential μ. The Fermi energy is defined by $E_F \equiv \mu(T = 0)$. It corresponds to the energy of the highest occupied state at $T = 0$ and defines the Fermi temperature $T_F = \frac{E_F}{k_B}$. The Fermi energy is given by the number of fermions in the trap and can be found by integrating the distribution over spatial and momentum coordinates:

$$N = \frac{1}{(2\pi\hbar)^3} \int \int d^3\mathbf{r} d^3\mathbf{p} f(\mathbf{r}, \mathbf{p}) \ . \tag{2.3}$$

For a three-dimensional harmonic trap,

$$V(\mathbf{r}) = \frac{1}{2} m(\omega_x{}^2 x^2 + \omega_y{}^2 y^2 + \omega_z{}^2 z^2) \ , \tag{2.4}$$

the Fermi energy can thus be calculated as

$$E_F = (6N)^{1/3} \hbar\overline{\omega} \ , \tag{2.5}$$

where $\overline{\omega} = (\omega_x \omega_y \omega_z)^{1/3}$ is the mean trapping frequency. E_F thus depends strongly on the trap parameters.

More information on ultracold Fermi gases in a trap can be found in [Joc09] and [Ket08].

2.2 Interactions in ultracold gases

After reviewing some properties of the non-interacting Fermi gas, interactions will now be introduced to the system. They are due to elastic scattering between the particles and can be resonantly enhanced by means of Feshbach resonances.

2.2.1 Elastic scattering in ultracold gases

Due to the low energy of the atoms and their long de Broglie wavelength, scattering in ultracold gases has to be treated quantum-mechanically. For a radially symmetric scattering potential between two atoms $V_{sc}(r)$, the Schrödinger equation reads:

$$\left[\frac{\mathbf{p}^2}{2m} + V_{sc}(r) \right] \phi(\mathbf{r}) = E\phi(\mathbf{r}) \ . \tag{2.6}$$

$\phi(\mathbf{r})$ can be divided into an incoming plane wave and a scattered spherical wave:

$$\phi(\mathbf{r}) = \phi_0(\mathbf{r}) + \phi_s(\mathbf{r}) = e^{ik_0 z} + f(\theta) \frac{e^{ikr}}{r} \tag{2.7}$$

where the scattering amplitude $f(\theta)$ contains all the information about $V_{sc}(r)$ and determines the differential scattering cross section:

$$\frac{d\sigma}{d\Omega} = \begin{cases} |f(\theta)|^2 & \text{non-identical particles} \\ |f(\theta) + f(\theta + \pi)|^2 & \text{identical bosons} \\ |f(\theta) - f(\theta + \pi)|^2 & \text{identical fermions} \end{cases} \tag{2.8}$$

For indistinguishable particles, there are two scattering processes which lead to the same result. This can be understood with the help of figure 2.1: although particle A and B are swapped for the two processes, it is not possible to measure which process occurred. Therefore, both processes have to be taken into account when calculating the scattering cross section. In the case of bosons, the total wave function has to be symmetric against particle exchange. For this reason, the two processes have to be added. For fermions, they have to be subtracted in order to obtain an antisymmetric wave function.
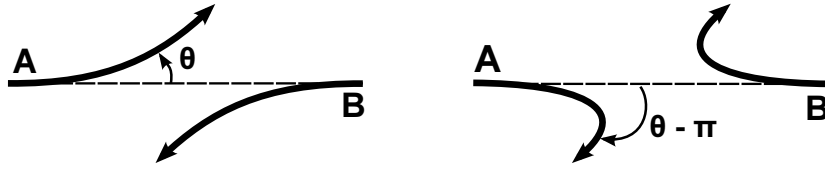

Figure 2.1: Scattering of two identical particles. Although the two possible processes are different, it is impossible to distinguish between them since particle A and B are identical. Both processes therefore have to be taken into account for the calculation of the scattering cross section.

Since $V(r)$ is radially symmetric, it is convenient to express (2.6) in spherical coordinates and do a partial wave expansion. A suitable ansatz for $\phi(\mathbf{r})$ is

$$\phi(\mathbf{r}) = \sum_{l=0}^{\infty} \frac{u_l(\mathbf{r})}{r} P_l(\cos\theta) \tag{2.9}$$

with the Legendre polynomials $P_l(\cos\theta)$. Solving for $u_l(\mathbf{r})$ leads to

$$u_l(\mathbf{r}) \propto \alpha_l \, \sin\left(kr - \frac{l\pi}{2} + \delta_l\right) \tag{2.10}$$

with the scattering phase shift δ_l between the incoming and scattered wave.

Plugging (2.10) into (2.9) and comparing the result to (2.7) yields

$$f(\theta) = \frac{1}{k} \sum_l (2l+1)\, e^{i\delta_l} \sin\delta_l\, P_l(\cos\theta) \ . \tag{2.11}$$

After integrating $\frac{d\sigma}{d\Omega}$ over the solid angle, the total scattering cross section is found to be

$$\sigma = \frac{8\pi}{k^2} \sum_l (2l+1)\, \sin^2\delta_l \tag{2.12}$$

for indistinguishable particles. For distinguishable particles, the prefactor is 4 instead of 8.

Taking into account the centrifugal barrier for an $-\frac{1}{R^6}$ interatomic potential (van der Waals potential), one finds that $\delta_l \propto k^{2l+1}$. Higher orders of l are therefore suppressed in ultracold gases, where k is always sufficiently small. They can therefore usually be neglected and equation 2.11 simplifies to

$$f(\theta) = \frac{1}{k} e^{i\delta_0} \sin\delta_0 \ . \tag{2.13}$$

The scattering amplitude for s-wave scattering does not depend on θ anymore and thus is spherically symmetric. Plugging this result into (2.8) leads to an important consequence: $\sigma \to 0$ for $k \to 0$ in the case of identical fermions. Thus, they do not scatter.

A one component ultracold Fermi gas therefore is a realization of an ideal (and thus non-interacting) Fermi gas. In order to add interactions to the system, one needs at least two different components. They can be realized as different species of atoms or as different spin states of the same species.

The scattering length

As shown in the above paragraph, all relevant parameters of the s-wave scattering process are contained in the momentum k of the scattering particles and the scattering phase δ_0. It is possible to expand δ_0 in powers of k^2 and thus to merge them into one single number which characterizes the scattering process. This number is called the scattering length a and is defined by

$$k\, \cot\delta_0(k) = -\frac{1}{a} + \frac{1}{2}r_0 k^2 + \mathcal{O}(k^4) + ... \ . \tag{2.14}$$

r_0 is the effective range of the scattering potential. In the limit $k \ll 1/r_0$, which is a reasonable assumption for ultracold gases, 2.14 simplifies to

$$a = -\frac{\tan\delta_0}{k} \ . \tag{2.15}$$

The total scattering cross section can now be found by plugging (2.15) into (2.12):

$$\sigma = \begin{cases} \frac{4\pi a^2}{1+k^2 a^2} & \text{non-identical particles} \\ \frac{8\pi a^2}{1+k^2 a^2} & \text{identical bosons} \\ 0 & \text{identical fermions} . \end{cases} \qquad (2.16)$$

There are two limits in which (2.16) can be simplified:

- For $ka \ll 1$, i.e. a weakly interacting gas, the total scattering cross section can be expressed as

$$\sigma = \begin{cases} 4\pi a^2 & \text{non-identical particles} \\ 8\pi a^2 & \text{identical bosons} \\ 0 & \text{identical fermions} . \end{cases} \qquad (2.17)$$

  This also gives an instructive picture for a: the total scattering cross section of two atoms with scattering length a can be compared to the geometric cross section of two scattering hard spheres with radius r, which is $\sigma_{geom} = 4\pi r^2$.

- In a strongly interacting regime, where $ka \gg 1$,

$$\sigma = \begin{cases} \frac{4\pi}{k^2} & \text{non-identical particles} \\ \frac{8\pi}{k^2} & \text{identical bosons} \\ 0 & \text{identical fermions} . \end{cases} \qquad (2.18)$$

More information on scattering theory can for example be found in [Nol06, Sch05, Wac05].

2.2.2 Tuning the scattering length: Feshbach resonances

One of the most formidable properties of ultracold Fermi gases is the existence of magnetic Feshbach resonances. They allow for tuning of the scattering length to arbitrary values by applying a homogeneous magnetic field.
In this paragraph, scattering resonances and Feshbach resonances will be explained briefly. Then, the concept of universality will be introduced. Afterwards, Feshbach resonances in the ^{6}Li system will be treated.

9

Feshbach resonances and the BEC-BCS crossover

As soon as a scattering potential supports bound states, the scattering cross section will be resonantly enhanced when the energy of a bound state (E_B) is close to the energy of the incoming particle, which we set to $E_{in} \equiv 0$. This is called a scattering resonance and can qualitatively be understood as a coupling between the bound and the unbound state [Sch05].

In the case of two scattering atoms, the scattering potential depends on their relative spin configuration. This can be understood with the help of figure 2.2(a): Two atoms are scattering in the so called *open channel* (black potential in figure
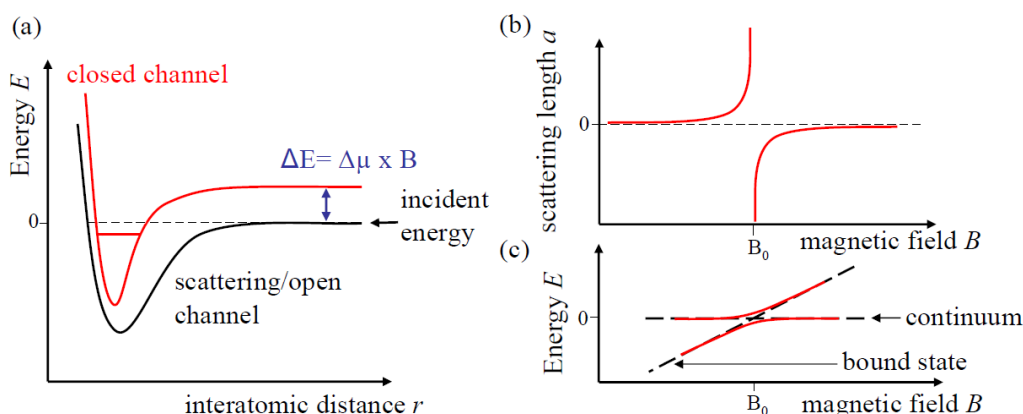

Figure 2.2: Origin of a Feshbach resonance.
Figure (a) shows the attractive potentials of the open and the closed channel. Their relative energies can be tuned against each other by applying a magnetic field.
Figure (b) shows the scattering length as a function of the magnetic field. At $B = B_0$, the open channel continuum and the closed channel bound state become degenerate and the scattering length diverges.
Figure (c) shows the relative energies of the open channel continuum and the closed channel bound state as a function of the magnetic field. On resonance, there is an avoided crossing between them.

2.2(a)). For a different spin configuration, there is a scattering potential with a higher continuum energy (red potential). It is called the *closed channel*, since it is not an allowed final state of the scattering process for reasons of energy conservation.

Since the two channels have different magnetic momenta μ, it is possible to tune their continua against each other by applying a magnetic field B:

$$\Delta E = \Delta\mu \cdot B \ .$$

$$(2.19)$$

10

This way, the bound state in the closed channel can be shifted with respect to the energy of the incoming atom in the open channel. The hyperfine coupling between the two channels becomes large when the energies of the open channel continuum and the closed channel bound state become degenerate ($E_B \to 0$). This leads to a resonantly enhanced scattering length and is called Feshbach resonance.

With the help of a Feshbach resonance it is thus possible to tune the scattering length a by applying a homogeneous magnetic field. Equation (2.20) describes the dependence of a on the magnetic field B [Moe95, Ino98]:

$$a(B) = a_{bg} \left(1 - \frac{\Delta}{B - B_0} \right) \quad . \tag{2.20}$$

a_{bg} is the background scattering length, Δ and B_0 are the width and position of the resonance. The shape of the resonance is shown in figure 2.2(b).

Figure 2.2(c) shows the Energy E_B of the bound state relative to the continuum:

- For $B < B_0$, the bound state lies below the continuum (as in fig. 2.2(a)). Here, the scattering length a is positive, which corresponds to a repulsive mean field between the atoms. This region is known as the BEC side, as bosonic molecules of two atoms exist and can condense.

- For $B = B_0$, the scattering length diverges to $\pm\infty$.

- For $B > B_0$, the bound state lies above the continuum. Thus, the formation of molecules is not possible. The scattering length is negative, which means that the mean field interaction is attractive. This region is called the BCS side, as two fermions with a weak attractive interaction are the basic assumptions Bardeen, Cooper, and Schrieffer made for their theory of superfluidity and superconductivity [Bar57].[1]

Looking more closely at 2.2(c), one can see that there is an avoided crossing between the bound and the unbound state. This is due to the coupling between the two states. The avoided crossing can be used to merge single atoms into molecules by adiabatically ramping down the magnetic field.

For $B \gg B_0$, $a < 0$ and $|a|$ is small. The fermions therefore weakly attract each other, but are also repelled from each other by the Fermi degeneracy pressure. As B decreases, a stays negative and $|a|$ increases. The attraction thus becomes stronger and the atoms are squeezed closer together. On the Feshbach resonance ($B = B_0$), a changes its sign. The interaction therefore also changes sign and becomes strong and repulsive. At the same time, the atoms form bosonic molecules. The degeneracy pressure therefore vanishes and the repulsive mean field takes its place,

---

[1]Indeed superfluid behavior of ultracold Fermi gases in this regime can observed.

keeping the molecules apart from each other and thus preventing condensation. As the magnetic field decreases further, $|a|$ decreases and the repulsion becomes weaker until the molecules condense into a molecular Bose-Einstein condensate.

This way, superfluid fermions can continuously be driven into a BEC of molecules.

Universality

As the scattering length can be tuned to arbitrary values with the help of Feshbach resonances, an interesting question arises: What happens if the scattering length is considerably larger than the effective range of the interaction potential r_0?

This question leads to the powerful concept of universality: in a regime where $a \gg r_0$, scattering processes can be described without knowledge of the actual shape of the interaction potential. It is therefore possible to describe all systems in this universal regime with the same physics, using only the scattering length a. Properties measured in any universal system can therefore be transferred to any other universal system.

In the case of ultracold ^{6}Li gases, the atoms interact with each other through the van der Waals force. For an atomic mass M, the range of the inter atomic scattering potential is therefore given as the van der Waals range:

$$r_0 = l_{vdW} = \left(\frac{MC_6}{\hbar^2} \right)^{1/4} . \tag{2.21}$$

For ^{6}Li, $l_{vdW} = 62.5a_0$ [Bra08]. By employing a Feshbach resonance, the scattering length can easily be tuned to much larger values. Thus, universal physics can be studied.

Feshbach resonances in the ^{6}Li system

For our experiment, we use ^{6}Li atoms in their lowest three hyperfine states (figure 2.3).

The ^{6}Li atom has a nuclear spin of $I = 1$ and an electron spin of $S = 1/2$. Hence, the $2S_{1/2}$ ground state splits into a hyperfine doublet ($F = 1/2$) and a quadruplet ($F = 3/2$) at low magnetic fields $B \ll 30G$ (Zeeman regime). At high fields ($B \gg 30G$) the nuclear spin decouples, so that there are three $m_S = -1/2$ states which are high field seekers (i.e. their total energy decreases with B), and three $m_S = +1/2$ low field seeking states. We will label the hyperfine states $|1\rangle$ through $|6\rangle$, according to figure 2.3.

The high field seeking states $|1\rangle$, $|2\rangle$ and $|3\rangle$ have energy differences of approximately 80 MHz. Atoms can be driven between them by applying radio frequency pulses.
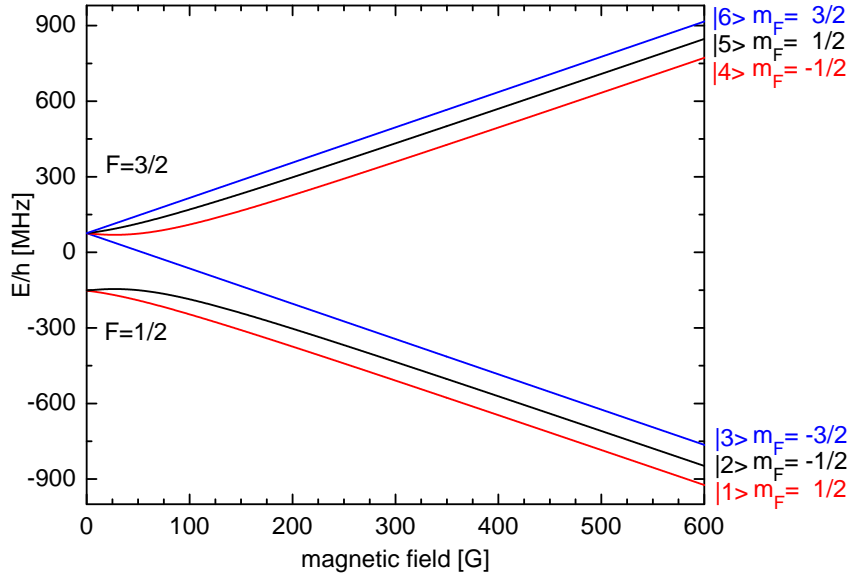
Figure 2.3: Energy splitting of the ground state of ^{6}Li in a magnetic field. As the magnetic field increases, the nuclear spin decouples and the $F = 1/2$ doublet and $F = 3/2$ quadruplet merge into three high field seeking and three low field seeking states.

As we want to use states $|1\rangle$, $|2\rangle$ and $|3\rangle$, three different scattering lengths are relevant in our system: a_{12}, a_{13} and a_{23}. Figure 2.4 shows them for magnetic fields up to $B = 1200G$. As one can see, they all have a Feshbach scattering resonance at roughly the same magnetic field. It is thus possible to tune all scattering lengths to large values at the same time. Also, the resonances are rather broad which allows the precise tuning of the scattering length.

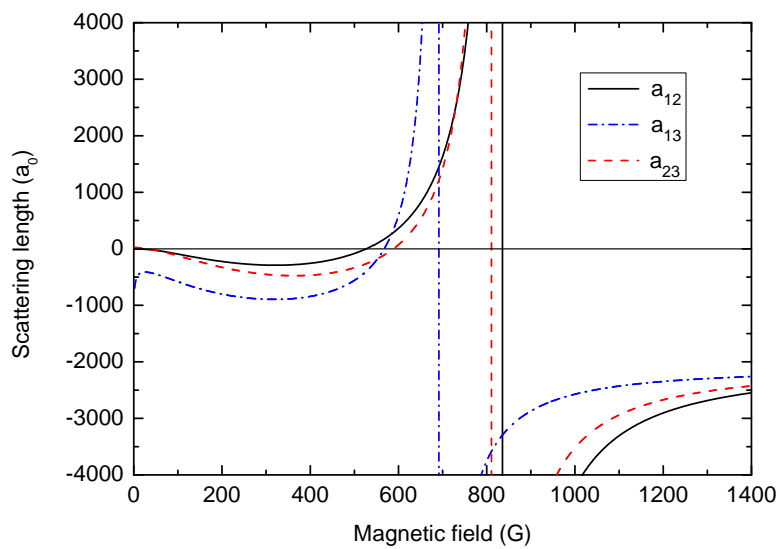More details on Feshbach resonances can be found in [Chi08].

Figure 2.4: Scattering lengths between ^{6}Li atoms in their three lowest hyperfine states. The scattering lengths are given in Bohr radii (a_0). Taken from [Jul].

Chapter 3

Laser Cooling of Atoms

For the quantum mechanical properties mentioned in chapter 2 to govern the behavior of a cold atomic gas, the wave functions of the single atoms have to overlap with each other. In order to fulfill this criterion, the phase-space density $\rho = n\lambda_{deb}^3$ of the gas has to approach unity.

In the case of a Fermi gas, quantum degeneracy is reached at $T \lesssim 0.5T_F$. Depending on the trap geometry and particle number, a typical value for T_F is approximately $1\mu K$.

These ultra low temperatures can only be achieved by combining several trapping and cooling stages. This chapter gives a brief overview over the techniques we are using and plan to use in the later stages of this experiment.

First, the interaction between atoms and light will be briefly discussed. Then its applications will be considered in the order they will be used in our experiment: atoms from the oven are slowed down by a Zeeman slower, trapped and cooled in a magneto-optical trap, and transferred into a dipole trap, where they are evaporatively cooled to quantum degeneracy. Table 3.1 gives an overview over some experimental parameters of these cooling stages.

At the end of the chapter, some details of the ^{6}Li system will be explained.

Stage of the experiment	Parameters	
oven	$T \approx 620\,\mathrm{K}$	
atom beam	$v \approx 1500\,\mathrm{m/s}$	$\rho = \mathcal{O}(10^{-10})$
Zeeman slower	$a_{max} \approx 2 \cdot 10^6\,\mathrm{m/s}^2$	$v_{final} \approx 50\,\mathrm{m/s}$
magneto-optical trap	$T \approx 140\,\mu\mathrm{K}$	$\rho = \mathcal{O}(10^{-5})$
optical dipole trap	$T < \mathcal{O}(1\,\mu\mathrm{K})$	$\rho = \mathcal{O}(1)$

Table 3.1: Experimental parameters during the cooling process. All numbers calculated in this chapter refer to our ^{6}Li system.

3.1 Atom light interaction

There are two fundamentally different forces that act on an atom in a light field, which both originate from photon absorption and emission cycles:

- The *dipole force* is due to the polarization of an atom by the light field, which can also be understood as virtual absorption and stimulated emission, whereas

- the *spontaneous force* is due to absorption and spontaneous emission.

The origin of the two forces can be understood with the help of a classical model [Gri00]: the oscillating electric field induces an oscillating dipole moment in the atom. The oscillation is damped by the radiative energy loss of the oscillating dipole moment.

The electric field of the laser beam is given as

$$\mathbf{E}(\mathbf{r}, t) = \hat{\mathbf{e}}\, E(\mathbf{r}) e^{-i\omega t} + \hat{\mathbf{e}}\, E(\mathbf{r}) e^{+i\omega t} \quad , \tag{3.1}$$

where $\hat{\mathbf{e}}$ denotes the polarization direction and ω the oscillation frequency. The induced dipole moment p in the atom is proportional to the electric field:

$$p = \alpha(\omega) E \quad , \tag{3.2}$$

where α is the complex polarizability of the atom. Thus, the oscillation of the dipole moment can be expressed as

$$\mathbf{p}(\mathbf{r}, t) = \hat{\mathbf{e}}\, p(\mathbf{r}) e^{-i\omega t} + \hat{\mathbf{e}}\, p(\mathbf{r}) e^{+i\omega t} \quad . \tag{3.3}$$

Calculating the radiative energy loss of an oscillating electron with the Larmor formula, one finds the damping factor Γ_ω.

$$\Gamma_\omega = \frac{e^2 \omega^2}{6\pi\epsilon_0 m_e c^3} \quad , \tag{3.4}$$

e and m_e are the charge and mass of the electron, ϵ_0 is the vacuum permittivity and c is the speed of light.

The system can now be described with the equation of motion of a damped driven harmonic oscillator with resonance frequency ω_0

$$\frac{e^2 E(t)}{m_e} = \ddot{p} + \Gamma_\omega \dot{p} + \omega_0^2 p \quad . \tag{3.5}$$

Solving for the polarizability yields

$$\alpha(\omega) = \frac{e^2}{m_e} \frac{1}{\omega_0^2 - \omega^2 - i\omega\Gamma_\omega} \quad . \tag{3.6}$$
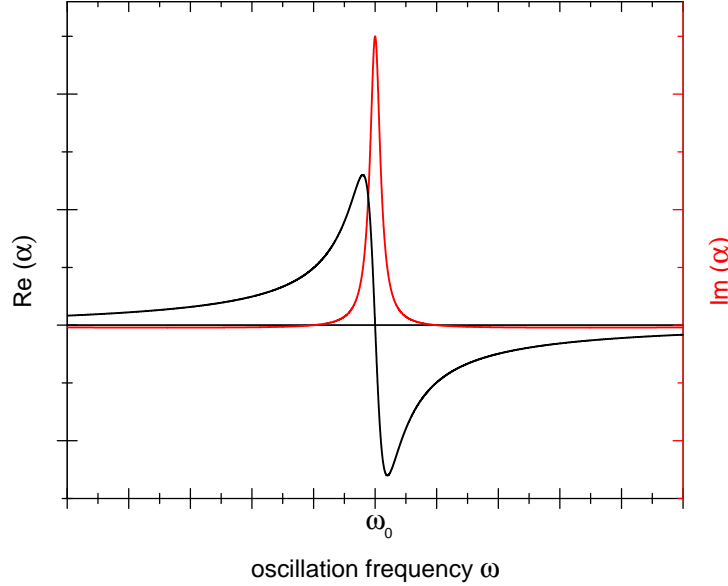
Figure 3.1: Real and imaginary part of the polarizability α of a harmonic oscillator. The axes are not to scale.

The two light forces are associated to the real and imaginary part of α, which is depicted in figure 3.1

Knowing α, it is now possible to calculate the light forces:

- The *dipole force* F_{dip} can be derived from the interaction potential between the light field and the induced dipole moment. Since the oscillation of the dipole moment is driven by the light field, F_{dip} is related to the driving term in (3.5) and the real part of α:

$$U_{dip}(\mathbf{r}) = -\frac{1}{2} \langle \mathbf{pE} \rangle \underset{I=2\epsilon_0 c|E|^2}{=} -\frac{1}{2\epsilon_0 c} \mathrm{Re}(\alpha) I(\mathbf{r}) \ , \qquad (3.7)$$

where $I(\mathbf{r})$ is the light intensity. Hence, the *dipole force* is given as

$$F_{dip}(\mathbf{r}) = -\nabla U_{dip}(\mathbf{r}) = \frac{1}{2\epsilon_0 c} \mathrm{Re}(\alpha) \nabla I(\mathbf{r}) \ . \qquad (3.8)$$

The ω-dependency of F_{dip} can be qualitatively understood from figure 3.1:

  - for $\omega < \omega_0$ (red-detuned light), F_{dip} is attractive as the dipole moment oscillates in phase with the light field. F_{dip} therefore points in the direction of the highest light intensity.

17

- For $\omega > \omega_0$ (blue-detuned light), it is repulsive and points away from the highest light intensity: There is a phase shift of π between the dipole moment and the field.
- On resonance ($\omega = \omega_0$), F_{dip} vanishes.

- The *spontaneous force* F_{spont} originates from the absorption and subsequent spontaneous emission of photons by the atom. Each time the atom absorbs a photon, it is excited and takes up a recoil momentum of $\hbar k$ in the direction of the light field. It then spontaneously re-emits a photon to a random direction. Since the momenta of the emitted photons cancel each other after several cycles, the total force on the atom only originates from absorption and points in the direction of the light field.

F_{spont} can be calculated from the photon scattering rate Γ_{sc}. The randomly scattered photons are lost from the directed light field. Therefore, the scattering rate can be calculated from the atom's power absorption P_{abs}, which is represented by the damping term in (3.5), and thus by the imaginary part of α:

$$P_{abs} = \langle \dot{\mathbf{p}}\mathbf{E} \rangle = \frac{\omega}{\epsilon_0 c} \mathrm{Im}(\alpha) I \tag{3.9}$$

$$\Gamma_{sc}(\mathbf{r}) = \frac{P_{abs}}{\hbar\omega} = \frac{1}{\hbar\epsilon_0 c} \mathrm{Im}(\alpha) I(\mathbf{r}) \ . \tag{3.10}$$

The net force on the atom can now be calculated from the scattering rate and the momentum transfer on the atom in each collision:

$$\langle \mathrm{F}_{spont} \rangle = \mathbf{p}_{phot}\Gamma_{sc} = \hbar\, \mathbf{k}_{phot}\Gamma_{sc} \ . \tag{3.11}$$

From figure 3.1, one can see that F_{spont} peaks on resonance, and approaches zero as $|\omega - \omega_0|$ increases. Unlike F_{dip}, it does not change its sign and therefore always points in the propagation direction of the laser beam.

Additional information on the spontaneous force can be gained from a quantum mechanical treatment of an atom in a light field [Met02]. Approximating the atom as a two-level system which can absorb photons from the light field and spontaneously emit them, one finds that

$$\Gamma_{sc} = \gamma\rho_{ee}, \tag{3.12}$$

where $\gamma \equiv 1/\tau$ is the linewidth of the excited state and ρ_{ee} is its population. For high light intensities I, ρ_{ee} will saturate to 1/2 as absorption and stimulated emission get into an equilibrium. It is therefore convenient to define the saturation parameter s_0:

$$s_0 \equiv \frac{I}{I_s} \ , \tag{3.13}$$

with the saturation intensity

$$I_s = \frac{\pi h c \gamma}{3\lambda^3} \ , \tag{3.14}$$

where λ is the transition wavelength.

The scattering rate Γ_{sc} can now be rewritten as

$$\Gamma_{sc} = \gamma \rho_{ee} = \frac{s_0 \gamma / 2}{1 + s_0 + (\frac{2\delta}{\gamma})^2} \ , \tag{3.15}$$

where δ is the total detuning of the light from the atom's resonance.

For $s_0 = 1$ and $\delta = 0$, the scattering rate is $\Gamma_{sc} = \gamma \,/\, 4$. For $s_0 \gg 1$, it will saturate to $\Gamma_{sc} = \gamma/2$. This leads to a power broadening of the atom's absorption curve:

$$\gamma' = \gamma\sqrt{1 + s_0} \ . \tag{3.16}$$

3.2 Application of the light force

Having discussed the properties of the light forces in section 3.1, it is now possible to understand the trapping and cooling devices in our experimental setup. Depending on which light force they employ, they can be divided into two groups:

- The Zeeman slower and the magneto-optical trap (MOT) employ the spontaneous force. The frequency of the light therefore has to be close to the atomic resonance. Since the transition frequency of an atom depends strongly on the magnetic field (Zeeman effect, see e.g. [Hak04]), it is possible to spatially modify the force by applying magnetic fields. This allows for the construction of sophisticated trapping devices.

  The main disadvantage of traps employing the spontaneous force is the existence of a lower temperature limit: since atoms in a MOT permanently absorb and re-emit photons, they jitter. It is therefore not possible to cool them below a temperature corresponding to this motion, which is called the Doppler temperature T_D.

  Both the Zeeman slower and the MOT are dissipative traps. An atom absorbs red-detuned photons which it sees as resonant due to its motion towards them. On average, it emits resonant photons: photons emitted in the direction of motion are blue-detuned, those emitted to the other direction are red-detuned. This way, the atom loses kinetic energy in each absorption and emission cycle. It is thus possible to cool a gas using just the spontaneous force. This technique is also known as Doppler cooling.

19

- The optical dipole trap uses the dipole force. There are two kinds of optical dipole traps: blue-detuned, repulsive dipole traps, and red-detuned, attractive traps. Since the scattering rate decreases quadratically with the detuning, it is useful to work with far-detuned lasers in order to minimize scattering.

  Due to the far detuning from the atomic resonance, the dipole force is practically independent of the magnetic field. Dipole traps are therefore suitable for experiments where additional homogeneous magnetic fields have to be applied to the atoms.

  Optical dipole traps have the big advantage that there is no limit to the temperatures which can be reached in them because they provide a conservative potential. Their main disadvantage is that it is hard to make them deeper than several μK. Thus, it is not possible to efficiently catch thermal atoms in them.

  Since the dipole potential is conservative, additional cooling methods like evaporative cooling can be used in order to cool a gas in a dipole trap.

Due to these advantages and disadvantages of each cooling and trapping device, a combination of them has to be used in order to efficiently trap atoms and cool them to quantum degeneracy.

3.2.1 Zeeman slower

As we want to do experiments in a shallow optical lattice, it is crucial for our setup to have a low background gas scattering rate and thus a low pressure ($\lesssim 10^{-11}$ mbar) in the experiment chamber. We therefore load the MOT with an atomic beam from an oven rather than from a background gas in the chamber.

Atoms leave the oven with a longitudinal velocity of $\overline{v} = \sqrt{\frac{8k_B T_{oven}}{\pi M}} \approx 1500$ m/s, where k_B is Boltzmann's constant, $T_{oven} = 350°$C, and M is the mass of a ^{6}Li atom. Thus, before they can be trapped they have to be slowed down to the capture velocity of the MOT (approximately 50 m/s). In our setup, this is done by a Zeeman slower. As mentioned above, it uses the spontaneous force:
A laser beam is directed towards the atomic beam from the oven, so that the atoms are decelerated by photon recoils. Since light and atoms are counterpropagating, the Doppler shift has to be taken into account and the light has to be red-detuned in order to be resonant. Also, as the atoms are being slowed down, the detuning has to be adapted to their current velocity.
Instead of changing the laser frequency in time, which would lead to bunches of slow atoms, it is convenient to tune the atoms' resonance frequency in space using the Zeeman shift. This can be done by applying a spatially varying magnetic field along the deceleration section, so that for each position (and thus velocity)

the atoms are resonant to the light. This technique leads to a continuous beam of slow atoms which can be trapped in the MOT.

For a Zeeman slower with a constant deceleration a, the atoms' velocity can be calculated from $v(t) = v_0 - at$ and $z(t) = v_0 t - \frac{a}{2} t^2$:

$$v(z) = v_0 \sqrt{1 - \frac{z}{z_0}} \ . \tag{3.17}$$

Since the Doppler shift is linear in v and the Zeeman effect is linear in B, the shape of the magnetic field has to be

$$B(z) = B_0 \sqrt{1 - \frac{z}{z_0}} \tag{3.18}$$

for a beam propagating in the z-direction through a magnet of the length z_0.

In addition to slowing the atoms down, the Zeeman slower also compresses their longitudinal velocity profile as the slowing force is velocity selective. The longitudinal temperature of the beam is therefore reduced. Thus, a combination of collimation apertures and a Zeeman slower already yields a precooled atomic beam.

More information on Zeeman slowing can be found in [Met02].

3.2.2   Optical molasses and MOT

In order to trap and cool a cloud of particles and thus to increase its phase space density, one needs two different forces:

- a confining force, which is position-dependent and pushes particles towards the center of the trap, and

- a damping force, which slows down moving particles and thus reduces the temperature of the cloud. Of course, this force also helps to confine particles in the trap.

In a magneto-optical trap (MOT), these two forces are both provided by the spontaneous light force of the same laser beams. This is done by a detuning of the light, its polarization and an inhomogeneous magnetic field. To understand how a MOT works, it is convenient to first look at the optical molasses, which provides the cooling force.

Optical molasses

In order to understand how the optical molasses works, it is instructive to consider the one-dimensional case. A three-dimensional optical molasses as used in our

setup can simply be constructed by perpendicularly superimposing three one-dimensional molasses.

A force which slows down an atom independently of its moving direction can be achieved with two counterpropagating, slightly red-detuned laser beams. For an atom at rest, the spontaneous force from both sides is the same, resulting in a total force of zero. As soon as the atom is moving to either direction, it is closer to resonance with the beam pointing against its motion due to the Doppler effect. The light force from this side therefore gets stronger than the one from the other side, which results in a total force that slows the atom down.

For counterpropagating beams with wave vectors $\pm\mathbf{k}$, which are red-detuned by $\delta_0 = \omega - \omega_0$, and an atom moving with velocity $+v$, the total detuning (in the atom's rest frame) amounts to

$$\delta_\pm(v) = \delta_0 \mp kv = \delta_0 \mp \omega \frac{v}{c} \quad . \tag{3.19}$$

Using equation (3.15), the total force acting on the atom can now be written as

$$\mathbf{F}_{OM} = \mathbf{F}_+ + \mathbf{F}_- = \frac{\hbar\mathbf{k}\gamma}{2}\left(\frac{s_0}{1 + s_0 + (\frac{2\delta_+}{\gamma})^2} - \frac{s_0}{1 + s_0 + (\frac{2\delta_-}{\gamma})^2}\right) \quad . \tag{3.20}$$

The velocity-dependence of the $\mathbf{F}_{OM}$ is depicted in figure 3.2: the dotted lines are the forces of each beam ($\mathbf{F}_\pm$). Their sum (solid line) is the resulting force $\mathbf{F}_{OM}$, which can be linearized for small velocities:

$$\mathbf{F}_{OM} \cong \frac{8\hbar k^2\delta_0 s_0}{\gamma(1 + s_0 + (\frac{2\delta_0}{\gamma})^2)^2}\mathbf{v} \equiv -\beta\mathbf{v} \quad . \tag{3.21}$$

The capture velocity of the optical molasses is defined by the two peaks of $\mathbf{F}_{OM}$, and thus given as

$$v_c^{OM} = \frac{\gamma}{k} \approx 4\,\frac{\mathrm{m}}{\mathrm{s}} \quad . \tag{3.22}$$

Considering equation (3.21), one might think that atoms in an optical molasses can be decelerated to $v = 0$, yielding a $T = 0$ gas. Unfortunately, this is not the case: (3.21) has to be understood as a time average of the cooling force. Looking at single absorption and emission processes, one will see that in each process, the atom's momentum is changed by the photon momentum $\mathbf{p} = \hbar\mathbf{k}$. This corresponds to an energy absorption of one recoil energy E_r in each absorption and emission process:

$$E_r = \frac{\hbar^2 k^2}{2M} = 4.90 \cdot 10^{-29}\,\mathrm{J} \,\widehat{=}\, 3.55\,\mu K \quad . \tag{3.23}$$

Each atom is therefore constantly heated by the ongoing absorption and emission process and conducts a random walk motion. By multiplying the recoil energy with the scattering rate Γ_{sc}, the heating rate can be found.
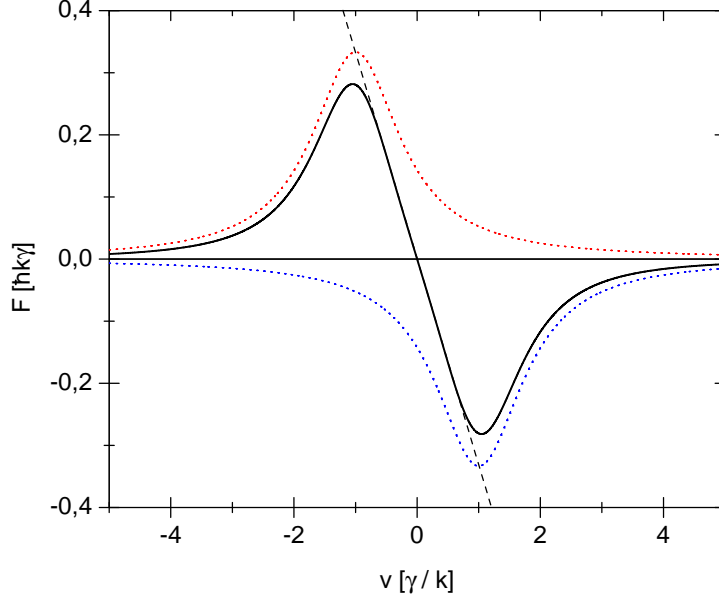
Figure 3.2: Force on an atom in a one-dimensional optical molasses as a function of γ/k. The curves were calculated for $s_0 = 2$ and $\delta_0 = \gamma$. The forces from the two counterpropagating beams $F_\pm$ (dotted lines) yield a total force F_{OM} (solid line) which changes sign for $v = 0$ and damps the atom's motion. For small velocities, F_{OM} can be linearized (dashed line).

Equating the cooling rate resulting from $\mathbf{F}_{OM}$ and this heating rate, one finds a thermal equilibrium at the so-called Doppler temperature [Met02]:

$$T_D = \frac{\hbar\gamma}{2k_B} = 137.6\,\mu K \tag{3.24}$$

with Boltzmann's constant k_B.

Although there are methods to cool a gas below T_D in an optical molasses or a MOT, they do not work for ^{6}Li. They rely on spatial changes of the absorption probability which are on the order of the trapping wavelength. These domains of high and low absorption probabilities are formed by interference of the trapping beams. Since ^{6}Li is very light, the atoms move too fast and do not stay in each domain for a period of time which is long compared to their scattering rate. For this reason, sub-Doppler cooling techniques cannot be used in our setup. They will therefore not be reviewed in this thesis.

MOT

As mentioned above, the optical molasses provides the cooling force and thus confines atoms in velocity space. In order to obtain a magneto-optical trap, confinement in real space has to be added. Therefore, a spatially selective force has to be added to the velocity selective force of the optical molasses. This can be done by exploiting the Zeeman splitting of different m_J states in a magnetic field and the selection rules for $\Delta m_J = \pm 1$ ($\sigma^\pm$ light).

Again, the one-dimensional case will be discussed. By perpendicularly superimposing the laser beams and magnetic fields, the concept can be expanded to 3 dimensions. A suitable magnetic field can be provided by two coils in anti-Helmholtz configuration.

In order to explain how a MOT works, it is convenient to consider a simple two-level system with $J_g = 0$ and $J_e = 1$ for the ground and excited states $|g\rangle$ and $|e\rangle$ (see figure 3.3). This is usually not the case in reality, but the same scheme also works for all $J_e = J_g + 1$ transitions.

To achieve a spatial dependence of the Zeeman splitting, a linear magnetic field gradient ($B(z) = A \cdot z$) is applied. The center of the trap is at zero field and thus at $z = 0$. The electronic energy levels of an atom then split up in the magnetic field and thus linearly tune with z. As the quantization axis of the atom is defined by the magnetic field B_{MOT}, it is flipped at $z = 0$. For this reason, the $m_J = -1$ state in figure 3.3 tunes to lower energies for positive and negative z, whereas the $m_J = +1$ state always tunes to higher energies.

In the case depicted in the figure, σ^- polarized laser beams are shined in from both sides. For zero detuning, both beams are resonant with atoms in the center of the trap. By red-detuning them by δ_0, the two resonant areas are shifted away from each other to $\pm R_c$. The beam coming from the left side therefore excites atoms at $z = -R_c$ to the $m_J = -1$ excited state, thus pushing them towards the center of the trap. After passing the center of the trap, the beam becomes resonant again at $z = +R_c$. However, since the quantization axis is flipped on that side, the polarization of the beam would have to be flipped as well in order to excite the atoms there. Thus, it cannot interact with atoms behind the center of the trap and push them out. The σ^- beam coming from the right side on the other hand only excites atoms at $z = +R_c$. Thus, a restoring force, which pushes all atoms towards the middle of the trap is created.

Using the same red-detuned beams as for the optical molasses, one gets a total detuning of

$$\delta_{tot\pm}(v,z) = \delta_0 \mp kv \pm \frac{\Delta\mu\,B(z)}{\hbar} \tag{3.25}$$

in the rest frame of an atom moving with velocity v. $\Delta\mu$ is the effective magnetic moment of the transition, which is the difference between the two involved
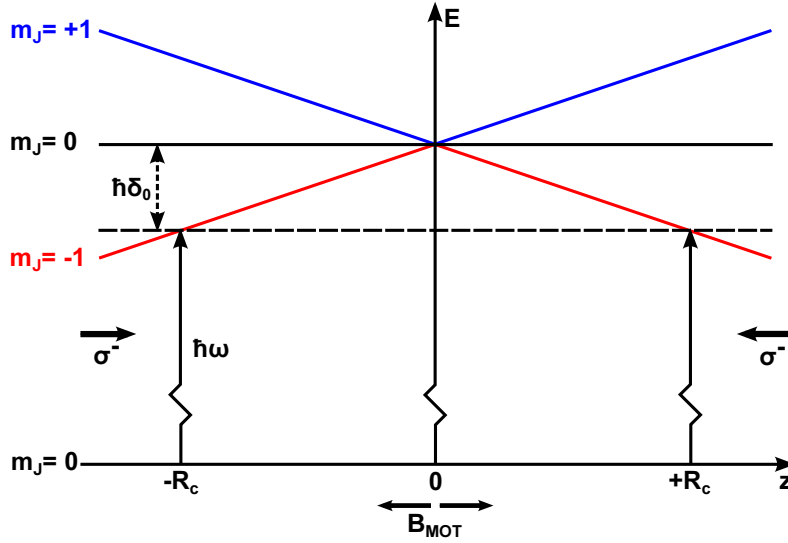
Figure 3.3: Concept of a MOT. Unlike in most figures found in literature, the z axis denotes real space. The helicity of the trapping beams is thus defined by their propagation direction. As the magnetic field B_{MOT} changes sign at $z = 0$, the quantization axis of the atoms (which is defined by B_{MOT}) is flipped there. The energy levels of the atoms thus tune to the same direction for positive and negative z (red and blue line). σ^- light coming from the left (right) side becomes resonant with atoms at $-R_c$ ($+R_c$). It therefore pushes them towards the center of the trap. On the far side of the trap, the laser beam cannot interact with the atoms due to its polarization.

magnetic momenta.

The force acting on atoms in the MOT can now be obtained by rewriting equation (3.20):

$$\mathbf{F}_{MOT} = \frac{\hbar\mathbf{k}\gamma}{2} \left(\frac{s_0}{1 + s_0 + \left(\frac{2\delta_{tot+}}{\gamma}\right)^2} - \frac{s_0}{1 + s_0 + \left(\frac{2\delta_{tot-}}{\gamma}\right)^2} \right) \quad . \tag{3.26}$$

Linearizing (3.26) leads to the atoms' equation of motion:

$$\mathbf{F}_{MOT} = -\beta\mathbf{v} - \kappa\mathbf{r} \tag{3.27}$$

with β from (3.21) and

$$\kappa = \frac{\Delta\mu}{\hbar k}\frac{\partial B}{\partial z}\beta \quad . \tag{3.28}$$

This equation of motion represents a damped harmonic oscillation of the atoms around the trap center: the confining force is always pointed towards the center

25

of the trap, acting as a restoring force, whereas the damping force of the optical molasses damps the oscillation. Since the damping rate $\Gamma_{MOT} = \beta/M$ is far greater than the oscillation frequency ω_{MOT}, the oscillation is overdamped. The atoms will therefore not oscillate in the trap but just be pushed to the center.

Just as for the optical molasses, the temperature limit of a MOT is given by the Doppler temperature $T_D \approx 140\mu K$ (3.24). This corresponds to a phase space density of approximately $\rho \approx 10^{-5}$, which is still 5 orders of magnitude away from unity. For our experiments, the MOT can therefore only serve as a first cooling stage, which creates an atomic gas that is cold enough to be loaded into a dipole trap. Quantum degeneracy can then be reached with the help of evaporative cooling.

Loading of the MOT and losses

The number of atoms in a MOT is determined by the loading and loss rates. It can be described by the following equation:

$$\frac{dN}{dt} = L - RN - \beta \int d^3r\, n(\mathbf{r})^2 \ . \tag{3.29}$$

N is the number of atoms in the MOT, n is their density. L is the loading rate of the MOT, whereas R and β describe one- and two-body losses.

In order to better understand equation (3.29), we will review these parameters:

- **Loading rate**

  The loading rate of the MOT depends essentially on the flux of the atomic beam and on the fraction of atoms that can be trapped. This fraction is mainly determined by the capture radius and the capture velocity of the MOT.

  The capture radius R_c of a MOT is defined by the distance from the center where an atom at rest is resonant to the MOT light (see figure 3.3). It can be expressed as

  $$R_c = \frac{\hbar\delta_0}{\Delta\mu\, \frac{\partial B}{\partial z}} \ . \tag{3.30}$$

  The maximum capture velocity v_c of a MOT (which must not be confused with the capture velocity of an optical molasses, v_c^{OM}) can be estimated from R_c and the spontaneous light force F_{spont} of the optical molasses. v_c is the highest velocity an atom can have and still be slowed down to $v = 0$ (and thus be captured) while flying through the MOT. The diameter of the MOT can be defined by twice its capture radius R_c, which leads to

  $$v_c < \sqrt{\frac{2R_c\mathrm{F}_{spont}}{M}} \ . \tag{3.31}$$

Since the atom cannot be resonant to the light throughout the whole slowing process, the actual force is smaller. Numerical simulations and experimental observations yield a capture velocity in the range of $v_c \approx 50$ m/s for a ^{6}Li MOT.

In our setup, where the Zeeman slower ends right in the center of the MOT (see 4.3.1), v_c mainly depends on the performance of the last part of the Zeeman slower. It can therefore be tuned by the detuning of the trapping and slowing light[1] and by the magnetic field gradient. The further detuned the light and the higher the magnetic field gradient is, the faster are the particles which get in resonance and can be slowed.

As a summary, one can therefore say that

- a greater $\frac{dB}{dz}$ increases v_c but at the same time decreases R_c and compresses the MOT, which leads to enhanced two-body losses.

- a greater detuning of the trapping light increases v_c and R_c, but lowers the scattering rate, which has a maximum for resonant light.

- **One-body losses**

One-body losses are due to collisions of a trapped atom with particles from the (hot) background gas or with the atomic beam used to load the MOT. In these collisions, atoms can pick up a kinetic energy that is higher than the depth of the trapping potential and therefore leave the trap. One-body losses can be reduced by decreasing the background pressure and by blocking the atomic beam after the MOT has been loaded.

- **Two-body losses**

Two-body losses are due to light assisted inelastic collisions of two trapped atoms. In such a collision, the atoms can gain enough kinetic energy to leave the trap. There are two important mechanisms for a two-body loss:

- In a *radiative escape*, an atom in the ground state ($2\,^2S_{1/2}$) and an atom in the excited state ($2\,^2P_{3/2}$) attract each other through their molecular potential $V_{SP} \propto -r^{-3}$. They are accelerated towards each other until the excited atom emits a photon and falls back into the ground state. The two ground state atoms now are in a flat potential V_{SS}, but still have the kinetic energy gained from the V_{SP} potential. This enables them to leave the trap. The emitted photon is red-shifted compared to the photon that drove the atom to the excited state. This way, energy from the MOT beams is converted into kinetic energy of the atoms.

---

[1]In our setup, the detuning of the Zeeman slower light and the MOT light cannot be changed separately, see also 4.2

– In a *state changing collision*, two atoms collide with each other and change their spin state. For example, both can go from the F = 3/2 branch of the ground state to the F = 1/2 ground state. The energy difference between the states is converted into kinetic energy.

The two-body loss rate is proportional to the squared atom density (n^2) in the MOT, and therefore plays an important role for high densities.

For a Gaussian shape of the atom cloud, the integral in (3.29) can be rewritten:

$$\frac{dN}{dt} = L - RN - \beta'N^2 \ , \tag{3.32}$$

where

$$\beta' = \frac{\beta}{(\pi/2)^{3/2}\sigma_z\sigma_r^2} \tag{3.33}$$

with the $1/\sqrt{e}$ widths σ_z and σ_r.

The rate equation (3.32) can now be solved for three regimes:

- For **low atom densities** in the MOT, two-body losses can be neglected. (3.32) then yields the loading curve

$$N_{load}^{lo-dens}(t) = \frac{L}{R}(1 - e^{-Rt}) = N_{max}(1 - e^{-Rt}) \ . \tag{3.34}$$

When the atomic beam is blocked ($L = 0$), the atom number decays exponentially:

$$N_{decay}^{lo-dens}(t) = N_0 e^{-Rt} \ . \tag{3.35}$$

- For **high densities**, two-body losses are dominant and have to be taken into account.

When the atomic beam is blocked and thus $L = 0$, (3.32) yields:

$$N_{decay}^{hi-dens}(t) = N_0 \frac{Re^{-Rt}}{R + N_0\beta'(1 - e^{-Rt})} \ . \tag{3.36}$$

This decay is faster than exponential as long as the density is high enough for two-body losses to play a role. For low densities, it merges into the exponential decay (3.35).

- In the **density limited** case, the density in the MOT saturates to n_0 and stays constant. A variation of the particle number then leads to a variation of the atom cloud's size instead of its density. Equation (3.32) therefore does not

hold in this case. Instead, the integral over the squared density in equation (3.29) can be solved for the constant density n_0 and (3.29) can be written as

$$\frac{dN}{dt} = L - (R + \beta n_0)N \ .$$
(3.37)

This yields the loading curve

$$N_{load}^{dens-lim}(t) = \frac{L}{R + \beta n_0}(1 - e^{-(R+\beta n_0)t})$$
(3.38)

and the decay curve

$$N_{decay}^{dens-lim}(t) = N_0 e^{-(R+\beta n_0)t} \ .$$
(3.39)

3.2.3 Optical dipole trap

For the planned experiments with our apparatus, we want to use atoms in an optical dipole trap and an optical lattice. The advantage of optical dipole traps is that it is possible to cool a trapped gas to degeneracy since there is no heating due to resonant light. Also, it is possible to apply almost arbitrary homogeneous magnetic fields to atoms in a dipole trap without affecting the trap.

Since the typical depth of a dipole trap is on the order of several mK, it is not possible to directly load the trap from a vapor or even a Zeeman slower beam. The atoms rather have to be precooled in a MOT and then transferred into a dipole trap for evaporative cooling.

For large detuning and negligible saturation, the dipole potential (3.7) can be rewritten in a more convenient form [Gri00]:

$$U_{dip}(\mathbf{r}) = -\frac{3\pi c^2}{2\omega_0^3}\left(\frac{\gamma}{\omega_0 - \omega} + \frac{\gamma}{\omega_0 + \omega}\right)I(\mathbf{r}) \ .$$
(3.40)

Writing the scattering rate in a similar way yields

$$\Gamma_{sc}(\mathbf{r}) = \frac{3\pi c^2}{2\hbar\omega_0^3}\left(\frac{\omega}{\omega_0}\right)^3\left(\frac{\gamma}{\omega_0 - \omega} + \frac{\gamma}{\omega_0 + \omega}\right)^2 I(\mathbf{r}) \ .$$
(3.41)

Whereas the dipole potential scales like $\frac{I}{\Delta\omega}$, the scattering rate scales like $\frac{I}{(\Delta\omega)^2}$. Since scattering leads to heating of the atoms or even atom loss (for shallow traps with $U_{dip} = \mathcal{O}(E_r)$), it is crucial to keep the scattering rate as low as possible. It is therefore favorable to use far detuned light with very high intensities in order to obtain a sufficiently strong trapping potential.

Dipole traps can be realized in a variety of geometries. For evaporative cooling, we will use a far red-detuned Gaussian beam which we will cross with its own

reflection in an acute angle, leading to a cigar-shaped trap. In order to prevent interference effects, the polarization of the reflected beam will be rotated with respect to the original beam. Afterwards we will load the cold atoms in a pancake-shaped dipole trap and finally into an optical lattice.

Evaporative Cooling

Since the dipole force is conservative, a dipole trap does not automatically cool atoms as a MOT or a Zeeman slower do. It is therefore necessary to use an additional cooling method in order to further increase the phase space density. However, the conservative potential of the dipole trap allows for forced evaporative cooling, which will briefly be reviewed here.

The basic idea behind evaporative cooling is to remove the hottest atoms from the trap, thus cutting off the tail of the thermal Boltzmann distribution. Afterwards, one allows the gas to re-thermalize, so that a new Boltzmann distribution (with a smaller mean temperature) can develop. As already mentioned in chapter 2.2.1, rethermalization requires scattering and therefore at least two different components (e.g. different spin states) of fermions in the trap.

Removing hot atoms can for example be done by decreasing the power of the trapping laser and thus lowering the trap depth. For a trap depth U, a fraction $exp(-U/k_BT)$ of the atoms can escape the trap.

By several cycles of evaporation and subsequent re-thermalization, the gas in the trap can be cooled to degeneracy.

More information on evaporative cooling can for example be found in [O'H01].

Optical lattices

A special application of the optical dipole trap are optical lattices. An optical lattice can be realized by retroreflecting a laser beam and thus letting it interfere with itself. This way, a standing light wave is created. For a red-detuned beam, atoms can thus be trapped in the anti-nodes of the standing wave, where the intensity has a maximum. The dipole potential of the standing wave is

$$U_{lat}(x) = U_0 \cos^2(k_{lat}x) \tag{3.42}$$

where k_{lat} is the wave vector of the lattice beam.

By overlapping several retroreflected beams, two- and three-dimensional lattices with various symmetries can be created. In order to obtain a stable lattice, the setup has to provide phase stability as drifting phases would shift the lattice sites.

An ultracold Fermi gas in an optical lattice is described by the Fermi-Hubbard Hamiltonian. For a two-component Fermi gas in the spin states $\sigma = |1\rangle, |2\rangle$, the

Hamiltonian is given as [Ess10]

$$\mathcal{H} = -J \sum_{\langle i,j \rangle, \sigma} \left(\hat{c}_{i,\sigma}^\dagger \hat{c}_{j,\sigma} + \hat{c}_{j,\sigma}^\dagger \hat{c}_{i,\sigma} \right) + U \sum_i \hat{n}_{i,|1\rangle} \hat{n}_{i,|2\rangle} \ . \qquad (3.43)$$

The lattice sites are numbered i, j, where $\langle i, j \rangle$ denotes neighboring sites. $\hat{c}_{i,\sigma}^\dagger$ and $\hat{c}_{i,\sigma}$ are the creation and annihilation operators for a particle with spin state σ in the lattice site i. The first term therefore describes tunnelling between neighboring lattice sites. The strength of this tunnel coupling is given by the tunneling energy J. The second term describes interaction between atoms in the same site with the particle number operator $\hat{n}_{i,\sigma}$ and the onsite interaction energy U.

Both J and U can be controlled experimentally. The tunneling rate J depends on the lattice depth and can thus be tuned by the lattice laser intensity. The interaction U between atoms can be tuned with the help of a Feshbach resonance. Hence, ultracold gases in optical lattices provide a very flexible system which can be used to simulate solid-state phenomena.

More information on optical lattices can for instance be found in [Ess10, Blo05].

3.3 Cooling ^{6}Li

In this section, the transitions we use for trapping ^{6}Li are presented. Since the nuclear spin decouples for high magnetic fields, the level schemes for the low field regime (reached in the MOT) and the high field regime (reached in the Zeeman slower) are fundamentally different (see figures 3.4 and 3.5). They are therefore treated separately.

Low field regime

To trap and cool ^{6}Li in our MOT, we use the D2 transition between the $2^2S_{1/2}$ ground state and the $2^2P_{3/2}$ second excited state (figure 3.4). The wavelength of the transition is approximately 671 nm.

Compared to the D1 transition, the D2 transition has the advantage that its saturation intensity $I_{sat} = 2.54$ mW/cm^2 is approximately three times lower. Whereas the hyperfine splitting of the excited state ($\Delta E_{HFS}^e = 4.4$ MHz) cannot be resolved as it is smaller than the natural linewidth $\gamma/2\pi = 5.9$ MHz of the transition, the hyperfine splitting of the ground state ($\mathbf{F} = 1/2, 3/2$; $\Delta E_{HFS}^g = 228.2$ MHz) is experimentally relevant. Both transitions are allowed, and thus no closed transition exists. Therefore, one needs two different laser wavelengths to address them both. In ^{6}Li, both transitions roughly have the same strength, so both of them are used for cooling and one needs approximately the same intensity of each.
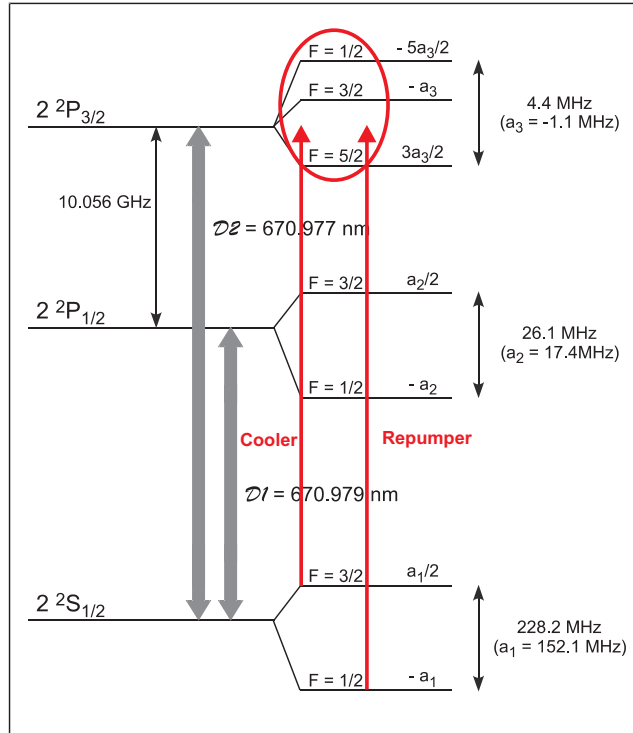
Figure 3.4: Level scheme of ^{6}Li with the transitions used for the MOT (not to scale). Whereas the three $2^2P_{3/2}$ states cannot be resolved, the two $2^2S_{1/2}$ can. The resulting two $D2$ transitions are labeled *cooler* and *repumper*. Taken from [Geh03].

As the F = 3/2 → F = 5/2 transition would be closed if the exited state could be resolved, it is labeled *cooler*, whereas the F = 1/2 transition is labeled *repumper*.

High field regime

For high magnetic fields ($B \gg 30G$) as used in the Zeeman slower, the nuclear spin **I** and the electron spin **J** decouple. **F** is therefore not a good quantum number anymore, which leads to a different level scheme with different transitions (see figure 3.5). In this regime, closed transitions can be achieved by driving atoms from the $m_S = +1/2$ branch of the $2S_{1/2}$ state into the stretched $m_J = 3/2$ ($m_L = 1$, $m_S = 1/2$) state. Since this transition has $\Delta m_L = +1$, it can be driven with σ_+ polarized light. It is closed because from the stretched state, the atoms cannot decay into the $m_S = -1/2$ branch of the $2S_{1/2}$ state due to the $\Delta m_S = 0$ selection rule.

Again, the m_I splittings in the excited state of the transition are too small to be
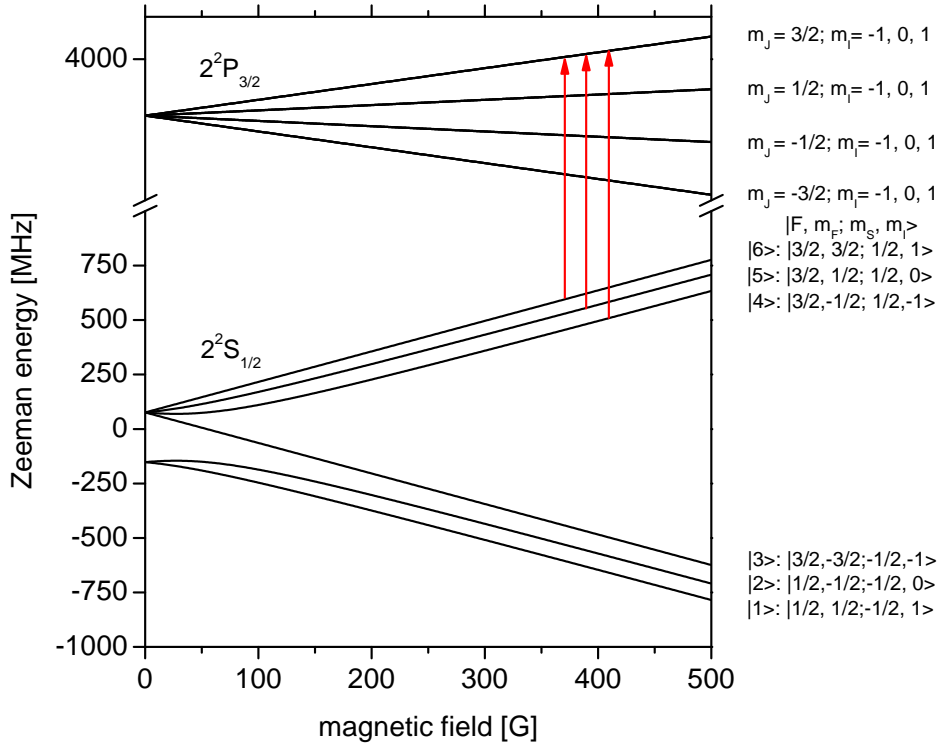
Figure 3.5: Level scheme of ^{6}Li for high magnetic fields with the transitions used in the Zeeman slower. Using the stretched $2^2P_{3/2}$, $m_J = 3/2$ state as an excited state allows for closed transitions.

resolved. The m_I splittings in the ground state are on the order of $\Delta E^g_{m_I} \approx 80$ MHz and thus resolvable. Still, it is not necessary to use three different wavelengths for the Zeeman slower light: with only one wavelength, each transition is driven for the corresponding velocity class.

Chapter 4

Experimental Setup

In this chapter, the experimental setup is described. Instead of a highly specialized apparatus, which can only be used for one specific kind of experiment, we wanted to build a very flexible machine. This way, it will be possible to use the apparatus for a long time and for many different experiments.

In order to reach this flexibility, we kept the design as simple as possible. This also has the advantage that fewer errors can occur and they can be tracked down more easily.

Another important point in our design is compatibility to our already existing apparatus. This way, devices that were constructed or bought for the old experiment can be used in the new one and vice versa. Also, when building the machine we could benefit from the experience with the old one. Many well-designed parts of the old apparatus could just be copied for the new one, whereas other parts were redesigned in order to further optimize them.

This chapter will first give an overview over the vacuum chamber and the laser system. Then, the trapping and cooling setup will be reviewed and the experiment control system will be briefly introduced.

4.1   Vacuum chamber

The vacuum chamber for our apparatus has to meet several requirements:

- Good optical access to the experiment chamber for high resolution imaging and the creation of an optical lattice.

- Ultra high vacuum in the experiment chamber for a long lifetime of atoms in our traps (recent publications on similar experiments report limitations of their imaging fidelity by collisions with the background gas [Bak10, She10]).

- Good access for magnetic coils for the MOT and Feshbach field.

- A high atom flux from the oven, which allows for fast MOT loading and thus fast experiment cycles.

- A simple design, which is at the same time robust and compact so it can be transported.

- The possibility of refilling the oven without breaking the vacuum in the main chamber.

In order to fulfill all these requirements, we opted for a design with the following properties:

- The core of the experiment chamber is a spherical octagon with six CF40 viewports and two custom made re-entrant CF100 viewports, providing good optical access and the opportunity to mount both the MOT coils and the Feshbach coils close to the atoms. Around the chamber, a large U-shaped aluminum breadboard provides room and stability for MOT and Zeeman slower outcouplers and additional optics (imaging system, dipole trap, and lattice).

- The apparatus is divided into two chambers, the experiment chamber and the oven chamber. They are separated by a differential pumping stage which ensures a low pressure in the experiment chamber when the pressure in the oven chamber is high due to outgassing of the hot oven. There is a gate valve between the two chambers. This way, the oven can be refilled without breaking the vacuum in the experiment chamber.

- An oven with a large aperture (5mm radius) and a short Zeeman slower provide enough flux to enable loading rates of $3 \cdot 10^8$ atoms/s and higher. It is thus possible to load enough particles for further experiments into the MOT within less than one second.

- The whole chamber is mounted on a separate aluminum breadboard with ITEM aluminum profiles. Thus, it is mechanically stabilized even if it has to be removed from the optical table it stands on.

Figure 4.1 provides an overview over the vacuum chamber which will be explained in detail in the next sections. An atomic beam from the oven (right side) is slowed down in the Zeeman slower (middle) and trapped in the octagon. The Zeeman slower beam enters the chamber through a viewport on the left side. A five- and a six-way CF100 cross connect the oven and the octagon to vacuum pumps, gauges, and valves.
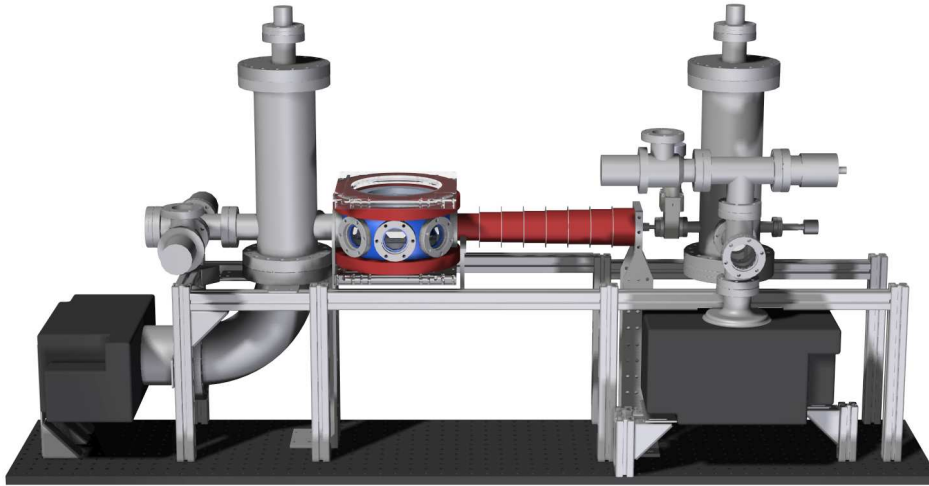
36

Figure 4.1: The vacuum chamber. The oven is on the right side of the setup. The Zeeman slower (red coils) connects the oven chamber and the experiment chamber (left side). Atoms are trapped in the spherical octagon (blue). The two CF100 towers serve as a gettering surface for the titanium sublimators and as a connection to the ion pumps (black), vacuum gauges, and valves.

4.1.1 The experiment chamber

As mentioned above, the main chamber of our setup is a spherical octagon with eight CF40 flanges and two CF100 flanges (KIMBALL PHYSICS). As we will need to apply well defined magnetic fields to control the scattering length with Feshbach resonances (see 2.2.2), it is made of non-magnetic type 316L steel.

Six of the CF40 flanges are equipped with zero profile viewports (UKAEA). They have a wavefront error of less than 80nm ($\sim \lambda/8$ for 671nm light) and are flat to 30 arcseconds. For an atom cloud in the middle of the chamber, they provide a numerical aperture of $NA_{hor} = 0.15$.

The two CF100 flanges are equipped with custom made re-entrant viewports (also UKAEA) with the same optical specifications. They provide a numerical aperture of $NA_{vert} = 0.88$. This allows for a theoretical maximum imaging resolution of $d_{min} = \frac{0.61\lambda}{NA} \approx 465nm$ (for 671nm light, Rayleigh criterion). They are also built in a way so that a NA = 0.6 objective, which was designed for our groups other experiment and is currently being manufactured, can also be used in this experiment.

As we use $\lambda = 671nm$ and $\lambda = 1064nm$ light for trapping, cooling and imaging, all viewports in our apparatus have a double V anti-reflective coating for these wavelengths.

As well as providing a high numerical aperture with relatively small (and thus less expensive) windows, the re-entrant design of the CF100 viewports allows us to later install a pair of Helmholtz coils, which we will use to apply a homogeneous field to control Feshbach resonances. Since the coils can be mounted close to the atoms, they can be comparably small ($d = R$ for Helmholtz configuration). This allows the creation of the required magnetic fields (up to 1500 Gauß) from relatively small currents (200 A), which will make fast switching easier. The Feshbach coils are currently being manufactured. More information on them is provided in the outlook (chapter 6.2).

The MOT coils are wound around the flanges of the re-entrant viewports and lie directly on the octagon. Figure 4.2 shows a cut through the octagon with the re-entrant viewports and the four coils.
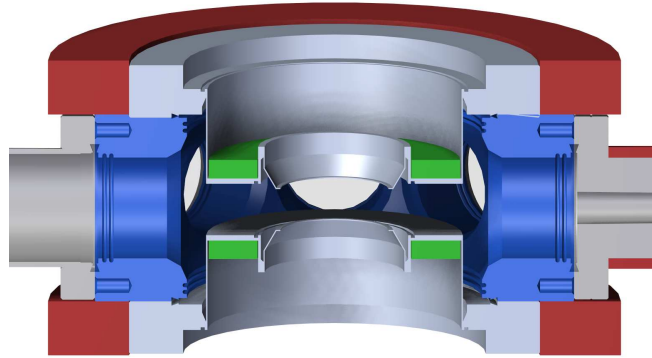

Figure 4.2: The octagon with the MOT coils (red) and the Feshbach coils (green). On the right side, the end of the Zeeman slower tube is connected to the octagon.

Since we want to drive transitions between different magnetic substates of the atoms with the help of radio frequency (RF) pulses (see also 2.2.2), we built an RF antenna into the main chamber. The main advantage of putting it into the chamber instead of outside is that it can be placed closer to the atoms and have an optimal orientation. This leads to stronger RF fields and thus higher Rabi frequencies at the same RF power. Also, the optical access through the bottom viewport would be reduced by an outside antenna.

The antenna consists of UHV rated $\varnothing$ 1mm capton insulated copper wire (MDC) and is held by grooves in the re-entrant viewports. Figure 4.3 shows the antenna as seen through one of the CF40 flanges of the octagon.

The Zeeman slower tube is attached to the main chamber. It is constructed as a double wall tube with integrated water cooling for the eight slower coils. More information on the Zeeman slower can be found in Philipp Simon's diploma thesis [Sim10], which will be published shortly after this work.
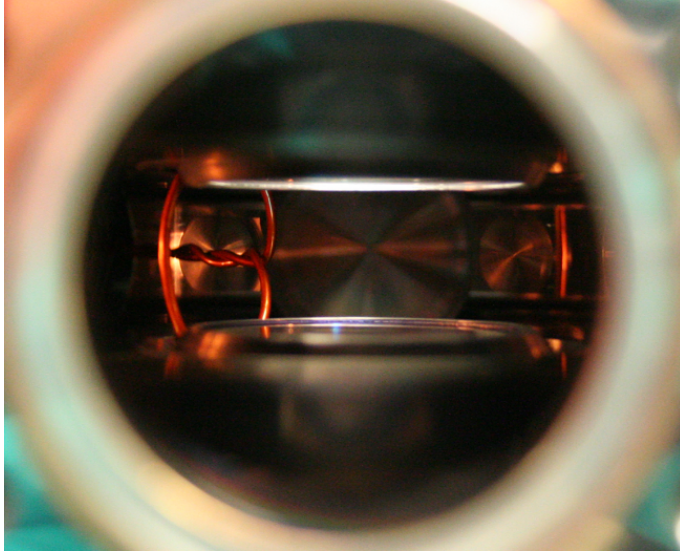
Figure 4.3: RF antenna in the main chamber. The windows of the re-entrant viewports can also be seen.

On the other side of the octagon, a 5-way CF100 cross is attached. It serves as a gettering surface for a titanium sublimator (see 4.1.3) as well as a connection to an ion getter pump, a vacuum gauge, the valve used for evacuation, and a feed through for the RF antenna. The Zeeman slower window is also attached to this unit.

4.1.2 The oven chamber

The layout of the oven chamber is shown in figure 4.4. The oven neck has a radius of $r = 5$mm and is $l = 45$mm long. At $T_{oven} = 350°$C, this leads to a total flux of

$$f = \frac{n\bar{v}\pi r^2}{4} \approx 10^{16}\,\text{atoms/s} \tag{4.1}$$

at an angle of

$$\alpha_{oven} = \arctan(\frac{2r}{l}) \approx 12.5° \quad, \tag{4.2}$$

assuming that the velocity of the ^{6}Li atoms follows the Maxwell-Boltzmann distribution

$$\bar{v} = \sqrt{\frac{8k_BT}{\pi M}} \approx 1500\,\text{m/s} \quad. \tag{4.3}$$

A second aperture ($d_2 = 5$mm), which is approximately 113 mm away from the end of the oven neck, reduces the opening angle of the atomic beam to $\alpha_{beam} \approx 3.5°$. At the same time, it protects the gate valve from being coated by the beam.
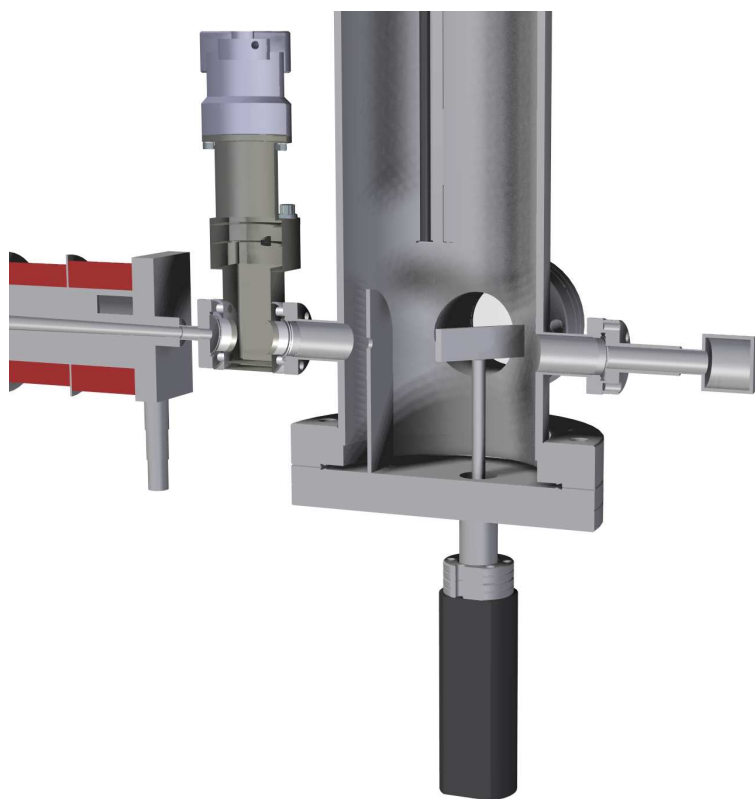
39

Figure 4.4: Oven chamber with aperture and beam shutter. The oven is on the right side. On the left side, the gate valve and a part of the Zeeman slower tube are attached. The titanium sublimator filaments hang above the aperture and the beam shutter.

The oven is filled with approximately 1 g of ^{6}Li. This should provide approximately 20,000 hours of operating time at $T_{oven} = 350°$C.

Between the oven and the second aperture, a polished stainless steel shutter can be rotated into the beam in order to block it after the MOT has been loaded. Thus, collisions of atoms in the trap with beam atoms are eliminated and the lifetime of atoms in the trap is increased. The backside of the shutter also serves as a mirror, with which the Zeeman slower beam can be reflected out of the chamber for adjustment purposes. It also allows for visual inspection of the oven.

4.1.3 Vacuum

In order to enable long lifetimes in our dipole traps, a very low pressure ($P_{exp} \lesssim 10^{-11}$ mbar) in the main chamber is necessary. This is achieved by the combination of several different getter pump systems. Getter pumps have the advantage over turbo pumps that they do not have any moving parts which create vibrations.

The experiment chamber is mainly pumped by a titanium sublimation pump (VARIAN) in the long part of the CF100 cross. Its pumping speed is proportional to the coated surface. In our setup, the surface is $A_{TSP} \approx 1000$ cm^2, leading to a pump speed of $S_{TSP} \approx 3100$ l/s for H$_2$ and similar values for other reactive gases. Since this type of pump only works for reactive gases, a STARCELL 75 (VARIAN) ion pump is added for non-reactive gases. At $P = 10^{-10}$ mbar, the ion pump has a pump speed of $S_{ION} \approx 20$ l/s for non-reactive gases like He or Ar.

In order to achieve the lowest possible pressure in the main chamber, the octagon itself is coated from the inside with a NEG (Non Evaporable Getter coating) from GSI [neg], which consists of a TiZrV alloy. It can be applied to a surface before evacuation and is activated during bakeout. Thus, it was possible to coat the octagon before assembling the vacuum chamber, which has the advantage that the viewports are not affected by the coating. The NEG coating has a pump speed of $S \approx 0.5$ l/s per cm^2 for H$_2$. The surface of the octagon is $A_{NEG} \approx 200$ cm^2, which leads to a total pump speed of $S_{NEG} \approx 100$ l/s. The main advantage of the NEG coating is that it getters particles right in the octagon and prevents outgassing from the octagon walls. Therefore, it significantly reduces pressure in the octagon although its total pump speed is small compared to the titanium sublimator.

The oven chamber is pumped by a titanium sublimator of the same size as the one in the experiment chamber and a slightly smaller STARCELL 40 pump ($\sim$15 l/s for He or Ar at $P = 10^{-10}$ mbar).

After 15 days of bakeout at approximately 200°C, we achieved a vacuum of $P_{exp} \approx 1 \cdot 10^{-11}$ mbar and $P_{oven} \approx 3 \cdot 10^{-11}$ mbar. We estimate the pressure in the octagon to be even lower due to the NEG coating.[1]

Since the main contribution to pressure in our system should be due to outgassing of the hot oven, the oven chamber is separated from the experiment chamber by a differential pumping stage built into the Zeeman slower tube. The tube is $l = 332$ mm long and conical to allow for a spread of the atomic beam. The radius at the oven side is $r_{oven} = 2.5$ mm and the radius at the experiment side is $r_{exp} = 6.1$ mm. Together with the average velocity $\overline{v}$ of Maxwell-Boltzmann distributed particles (see equation (4.3)), these numbers yield the tube's conductivity [Wut00]:

$$C = \frac{\pi r_{oven}^2 \overline{v}}{4} \frac{1}{1 + \frac{r_{oven} + r_{exp}}{4 r_{exp}^2} l} \approx 0.4 \, \text{l/s} \qquad (4.4)$$

---

[1]Since there is no vacuum gauge in the octagon, we cannot directly measure the pressure there.

for thermal H_2 atoms at room temperature. For heavier and thus slower molecules, the conductivity is lower.

Comparing this number to the total pump speeds of our system, one can see that it is possible to keep the 10^{-11} mbar vacuum in the experiment chamber even with a considerably higher pressure in the oven chamber.

Figure 4.5 shows the pressure in the oven chamber and the experiment chamber in dependence of the oven temperature. As expected, when the oven shutter is closed the pressure in the experiment chamber stays approximately constant as the pressure in the oven chamber increases by about one order of magnitude. When the oven shutter is open, the pressure in the experiment chamber increases by approximately a factor of 2. This is due to the atomic beam, which crosses the differential pumping stage and in addition to ^6Li also contains residuals from the oven.
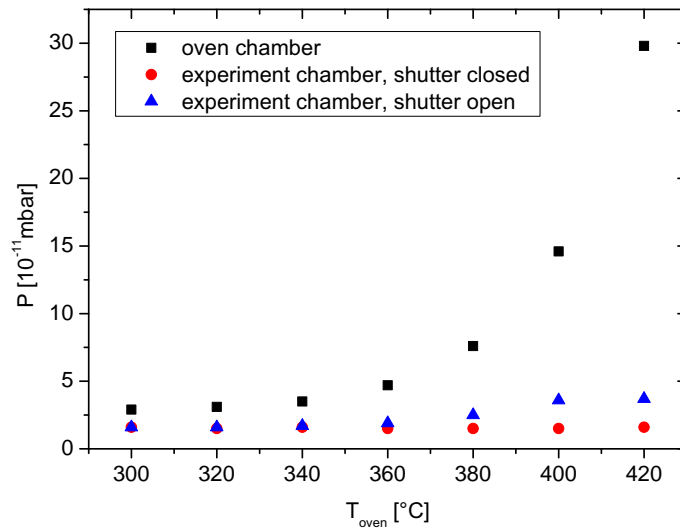

Figure 4.5: Pressure in the experiment and oven chamber as a function of the oven temperature. Whereas the oven pressure increases by approximately a factor of 10 as the oven is heated, the pressure in the experiment chamber increases by only a factor of 2 when the shutter is open and stays constant when it is closed.

At an oven temperature of 350°C, the pressure in the oven chamber is increased by approximately a factor of 1.5. In the experiment chamber, no significant increase in pressure can be seen at this temperature even with the shutter open. Still, collisions with background (and beam) atoms should be drastically increased compared to a closed shutter as the atomic beam passes right through the trap.

4.2 Laser system

In order to trap atoms in the MOT and to do fluorescence and absorption imaging, we need a laser system which provides the light. It has to fulfill several requirements:

- The laser frequency has to be tunable in a reliable and precise way.

- The linewidth of the lasers has to be considerably smaller than the linewidth of the cooling transition in order to precisely resolve the transition.

- The laser system has to provide enough laser power for trapping and imaging the atoms.

- The lasers have to stay in lock for as long as possible to allow for long, automatic experiment sessions.

- The setup should be as simple as possible, and thus easy to set up, debug and maintain.

- It has to be flexible and expandable for future changes.

To fulfill these requirements, we built a system which uses two separate grating stabilized diode lasers (TOPTICA) for trapping and imaging. These lasers have the following advantages:

- The grating stabilization allows for a wide tuning range of more than 10 GHz and relatively simple frequency stabilization.

- They provide a linewidth of less than 1 MHz, which is small compared to the natural linewidth of ^{6}Li: $\gamma = 5.9$ MHz.

- Diode lasers are considerably easier to maintain and cheaper than dye lasers, which are the only commercially available alternative at the required wavelength ($\lambda \approx 671$ nm).

For the MOT and Zeeman slower beams, we use a TA PRO system, which consists of a diode laser (DL PRO) and a tapered amplifier (TA). It provides approximately 350 mW laser power at 671 nm. For the absorption imaging beam, we will use a DL PRO laser, which provides approximately 15 mW.

 The laser system is set up on a separate optical table. After preparation, each beam is coupled into a single-mode polarization-maintaining optical fiber and transferred to the experiment table. Outcouplers then produce the required beam size and collimation and directly shine the light into the experiment chamber.

This fiber based design has the disadvantage that approximately half the laser power cannot be coupled into the fibers and is therefore lost. Still, it makes sense to use it for two reasons:

- Light from a single-mode fiber is always in a clean TEM 00 Gauß mode. This way, the irregular beam profile of light from the laser diodes does not affect the performance of the trapping and imaging setup.

- The laser preparation and the experiment itself are decoupled: it is possible to adjust or even completely change the setup on the laser table without changing the beam geometry in the experiment. Also, mechanical vibrations from the experiment table cannot be transferred to the laser table, where they might knock a laser out of the lock.

Optical setup

Figure 4.6 shows our 671nm laser system. The light from the TA PRO is split up into two beams, one for the cooler and one for the repumper. After adjusting the beam size, the cooler and repumper wavelengths (frequency difference: 228 MHz, see chapter 3.3) are created by shifting the beam frequencies by -114 MHz (cooler) and +114 MHz (repumper) in acousto-optic modulators (CRYSTAL TECHNOLOGY 3100-125). The two parts of the beam are superimposed again and then split into a Zeeman slower beam and three MOT beams. The Zeeman slower beam is red-detuned by approximately -70 MHz in another AOM (CRYSTAL TECHNOLOGY 3080-125) and coupled into a fiber, whereas the three MOT beams are directly coupled into fibers.

The imaging light from the DL PRO is put through a (CRYSTAL TECHNOLOGY 3080-125) AOM and then coupled into a fiber. The AOM is used as a fast switch to create short light pulses (down to several μs), which are necessary for a high time resolution for time of flight imaging.

In order to block single beams while they are not needed, we use laser shutters made of small loudspeakers (figure 4.7, page 46). More details on the shutters and their drivers can be found in [Zür07].

polarizing beam splitter   anamorphous prism pair

50/50 nonpolarizing beamsplitter   acousto-optic modulator

mirror   fiber coupler

beam sampler   laser shutter

$\lambda/2$ wave plate   lens

$\lambda/4$ wave plate   attenuator

photo diode

imaging beam

- 80 MHz

DL Pro

optical isolator

reference beam

Cavity

beat spect-imaging

TA Pro

TA

DL Pro

beat spect-trapping

to wavemeter

Zeeman slower

- 70 MHz

MOT beam 3
(vertical)

f = 125   f = 75   - 114 MHz

MOT beam 1
(horizontal)

f = 125   f = 75   + 114 MHz
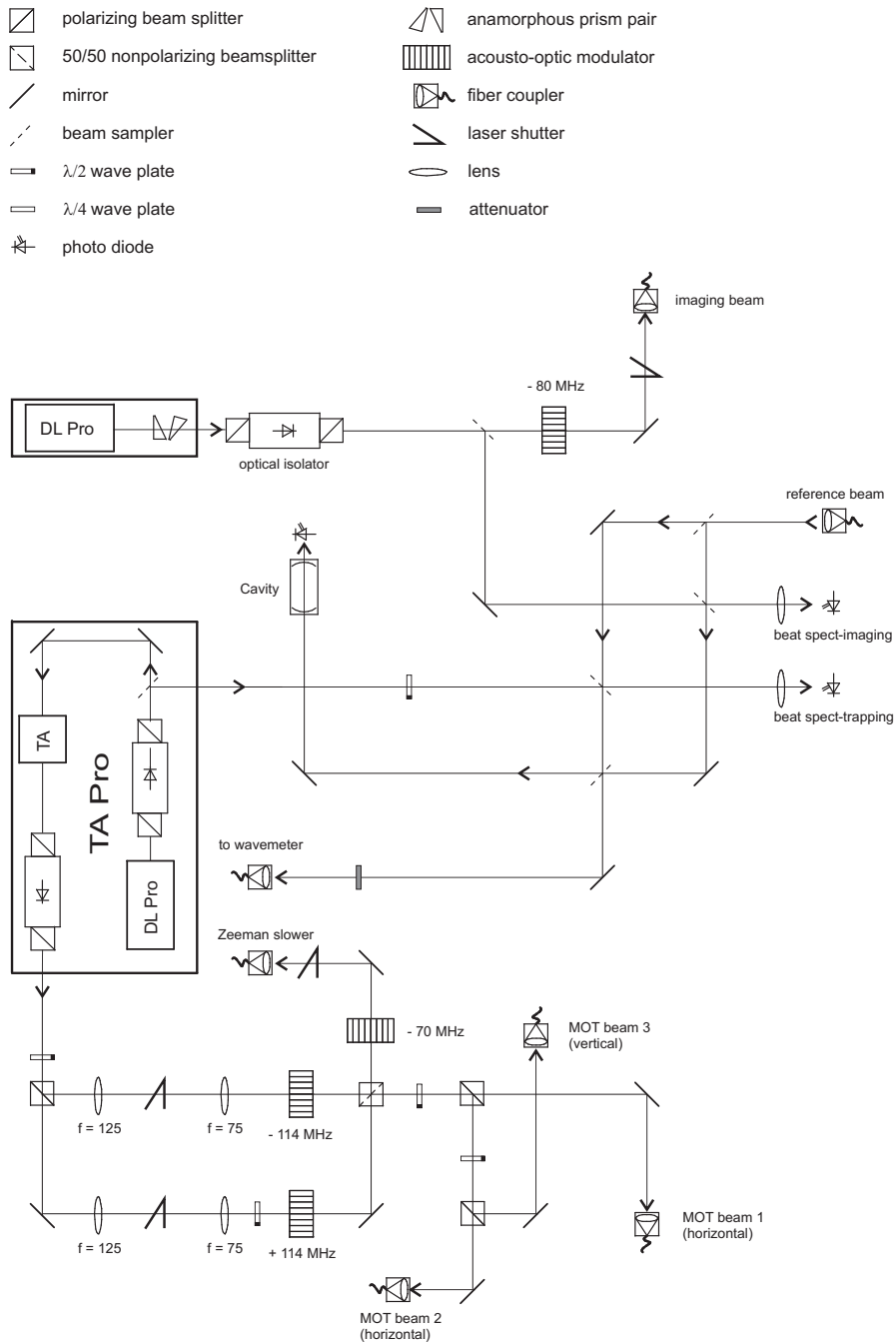
MOT beam 2
(horizontal)

Figure 4.6: The laser system. The upper part of the setup is used for frequency stabilization and diagnostics. Light from the two diode lasers is beat locked to light from the external reference beam with the help of photo diodes. The lower part of the setup is used to create the MOT and Zeeman slower beams, which are then coupled into optical fibers.
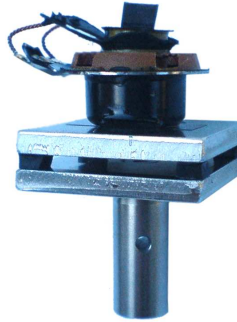
45

Figure 4.7: Laser shutter. A small loudspeaker is used to move the beam shutter. It is mounted on two aluminum plates which are connected by damping material in order to minimize noise transfer to the optical table.

Frequency stabilization

The laser frequency can be adjusted and stabilized with a grating which serves as one side of the laser resonator. It is tilted in a way so that the first diffraction maximum is reflected back into the resonator. By changing its angle and position with a piezo, the resonator mode - and thus the emission frequency - can be tuned. It is therefore possible to stabilize the laser frequency to a desired value by dynamically adjusting the grating with the piezo.

Both lasers are stabilized by beat locking them to a reference beam. This reference beam is created by an additional DL 100 laser and has already been set up for our other experiment. It is stabilized to the ^{6}Li F = 3/2 D2 transition (cooling transition, see chapter 3.3) by employing Doppler free FM spectroscopy on a vapor cell [Ser07].

A sample of the reference beam is coupled into an optical fiber and transferred to the optical table. There, it is split up and separately superimposed with a sample from each laser. The two beams interfere with each other and create a beating signal, which is recorded by a photodiode (TA PRO: HAMAMATSU 59055, bandwidth up to 1.5 GHz, DL PRO: HAMAMATSU G4176-03, 30 GHz). The frequency of the laser is then stabilized with respect to the reference beam using the beat offset lock principle explained in [Sch99]:

The beat signal (ω_b) recorded by the photodiode is amplified and mixed with an external frequency from a voltage controlled oscillator (ω_{VCO}). The mixer multiplies the two oscillations and therefore yields their sum and difference:

$$U_{mixer} \propto \cos(\omega_b t) \cdot \cos(\omega_{\mathrm{VCO}} t) = \frac{1}{2} \left(\cos((\omega_b - \omega_{\mathrm{VCO}})t) + \cos((\omega_b + \omega_{\mathrm{VCO}})t) \right) \ .$$
(4.5)

The frequency difference term is selected by a low pass filter and then split up. One part is sent through a delay line (realized by a coaxial cable with length $l = 2$m),

where it picks up a phase shift $\Phi = \frac{\Delta\omega\, l}{c}$. Then, it is mixed with the undelayed part again. After another low pass filter, the signal only depends on the phase shift and thus on $\Delta\omega$:

$$U_{error} \propto \cos\left(\frac{\Delta\omega\, l}{c}\right) \quad . \tag{4.6}$$

The laser is locked on a zero crossing of this error signal with a PID controller. By tuning ω_{VCO}, the offset of the laser frequency from the reference beam can now be adjusted.

The trapping laser is blue-detuned from the reference beam by 114 MHz. This way, its wavelength is right in the middle between the cooler and the repumper transition. Cooler and repumper light can thus be created by symmetrically shifting the wavelength by $\pm$ 114 MHz in two acousto-optic modulators (AOMs).

More details on our beat lock can be found in [Zür09].

For frequency diagnostics, beams from each laser are also coupled into a scanning Fabry-Perot cavity (THORLABS SA200-6A) and a wavelengthmeter (HIGH FINESSE WS7).

4.3   Trapping and cooling setup

4.3.1   Zeeman slower

The Zeeman slower we use in our setup has a decreasing field configuration. This means that the magnetic field decreases from the beginning of the slower tube towards the MOT. The last part of the slower field is provided by the MOT coils. Hence, the slower field goes down to B(z=0) = 0 and only ends at the very center of the MOT. Expansion of the atomic beam is thus reduced to a minimum, and very few slow atoms can get lost. This enables high MOT loading rates at moderate oven temperatures. In addition, a Zeeman slower which uses the MOT coils can be built shorter, which leads to a higher atom flux and a more compact, more robust vacuum chamber.

Although this configuration has the above mentioned advantages, there are some drawbacks to it: compared to e.g. a spinflip configuration Zeeman slower, where the magnetic field is zero in the middle of the slower tube, much higher magnetic fields are needed. This of course leads to more heating of the slower coils. For this reason, they have to be water cooled.

With the MOT-field included, our Zeeman slower is 40 cm long. It consists of 8 separate coils that are wound on the differential pumping tube between the oven chamber and the octagon. The tube also serves as a heat sink: Between the vacuum tube and the outer wall, there are four water cooling channels. Figure 4.8 shows the tube with the coils.
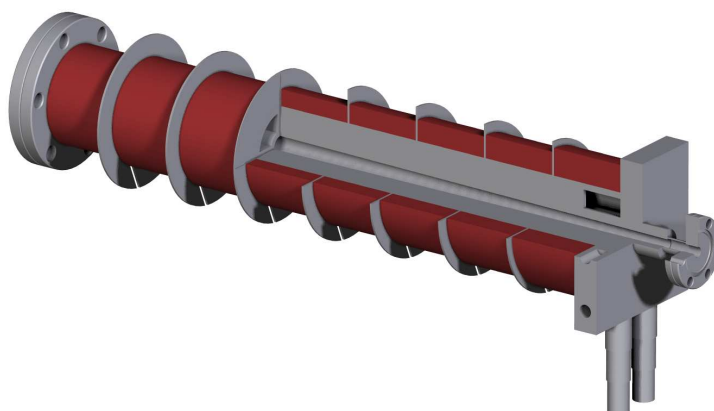
47

Figure 4.8: The Zeeman slower. The vacuum tube and water cooling channels for the coils are combined in one element.

The Zeeman slower light is shined in through a window at the end of the experiment chamber. The beam is fitted to the opening angle of the slower tube. It has a diameter of 23,5 mm at the window and focuses at approximately 1100 mm. This is achieved by an outcoupler with two f = 200 mm lenses.

The power of the Zeeman slower beam is 63 mW (46 mW cooler, 17 mW repumper), which corresponds to an intensity of approximately 80 mW/cm^2 on the octagon side of the slower tube and thus a saturation parameter $s_0 \gtrsim 30$ along the slower tube. The transition is thus highly saturated, which leads to the saturated scattering rate of $\Gamma_{sc} = \frac{\gamma}{2} \approx 18$ MHz. Due to the high saturation, the atoms' absorption curve is power broadened and therefore the slowable velocity class of atoms is extended.

In order to enable the closed transitions in the high field regime explained in 3.3, the Zeeman slower light has to be circularly polarized (σ_+). This is done with the help of a $\lambda/4$ waveplate built into the outcoupler.

As can be seen from figure 4.6 and table 4.1, the Zeeman slower light consists of both cooler and repumper light, although the transition in the high field is closed. This is done as the magnetic field of the slower goes down to zero and the light thus also has to drive the non-closed low field transitions.

More details on the Zeeman slower can be found in [Sim10].

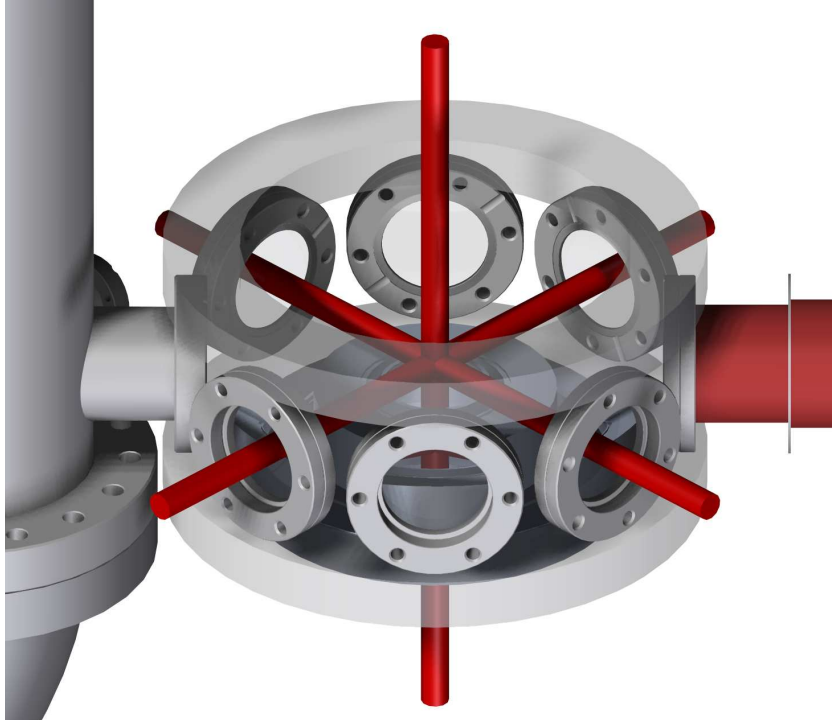### 4.3.2 Magneto-optical trap

Figure 4.9: Octagon with MOT coils (transparent gray) and MOT beams (red). On the right side, the Zeeman slower is attached to the octagon. The Zeeman slower beam comes from the left side.

Figure 4.9 shows the octagon with the MOT coils and beams. As mentioned above, the anti-Helmholtz MOT coils are wound around the flanges of the re-entrant viewports in a way so that they lie directly on the octagon. They consist of four stacked coils with 25 windings each and are made of 5 mm $\times$ 1 mm capton insulated copper wire. The wire is glued together with thermally conductive epoxy (EPO-TEK T7110). The coils are glued onto water cooled copper heat sinks. At $I = 34$ A, they provide a magnetic field gradient of $dB/dz \approx 30$ Gauß/cm across the MOT region. Figure 4.10 shows the shape of the field.

As shown in figure 4.9, the three MOT beams are shined in perpendicular to each other. They have a $(1/e^2)$ diameter of 11 mm. The two horizontal beams have σ^- polarization, the vertical one σ^+. All beams are provided by outcouplers with one f = 50 mm lens. After crossing the chamber once, each beam is retroreflected. The polarization is flipped by a $\lambda/4$ waveplate, which the beam passes before and after reflection.

The beams consist of cooler and repumper light with a power of approximately
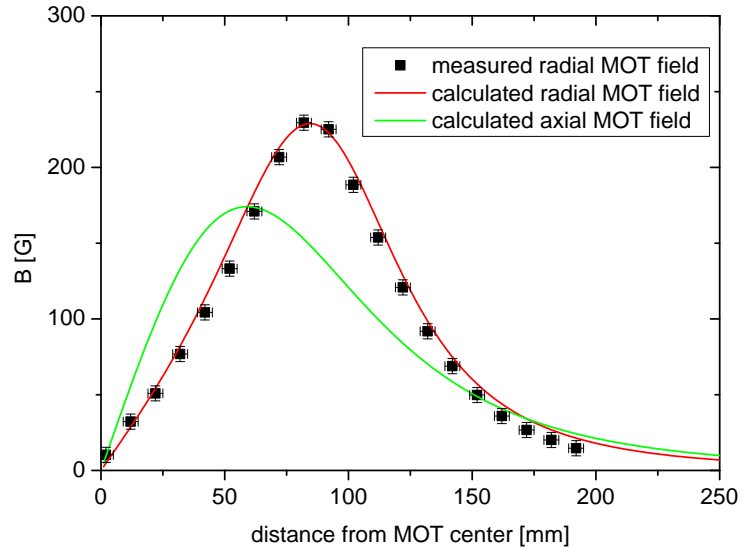
Figure 4.10: The magnetic field of the MOT as a function of the position. The field was measured using a Hall probe. The red curve indicates the calculated radial field, the green curve the calculated axial field.

10 mW each. Table 4.1 shows the exact values for each beam. The average saturation parameter is $s_0 \approx 8$, leading to a scattering rate of $\Gamma_{sc} = \frac{4}{9}\gamma \approx 16$ MHz for resonant atoms. Since the beams have a Gaussian intensity distribution, the saturation parameter in the beam middle is greater than the average by a factor of 2. Thus, the scattering rate in the middle of the beams is approximately $\frac{8}{17}\gamma$. The beams are red-detuned from the resonance by 40 MHz.

Beam Nr	Orientation	Power cooler	Power repumper	Total power
1	horizontal	14.7	10.3	25.0
2	horizontal	11.7	8.3	20.6
3	vertical	13.1	9.1	22.2
4	Zeeman slower	46	17	63.0

Table 4.1: Laser power of the MOT beams and the Zeeman slower beam.

4.4 Experiment control system and imaging setup

The apparatus is controlled by an automatic experiment control system. It has digital and analog output channels and is currently used for several tasks such as controlling beam shutters for laser beams and the atomic beam, switching magnetic fields for the MOT and the Zeeman slower on and off, controlling the beam detuning by adjusting VCO frequencies in the beat lock electronics and triggering the camera.

The experiment control system is implemented with FPGA controlled digital and analog I/O boxes. The FPGAs are programmed with the help of a LabView user interface. A versatile modular structure and an auto run function allow for automatic sessions of data-taking.

More information on the experiment control system can be found in Philipp Simon's diploma thesis [Sim10].

The LabView user interface also controls the imaging system and evaluates the data taken with a CCD camera (ALLIED VISION TECHNOLOGIES Stingray F-125B).

The camera has a resolution of 1292×964 pixels with a pixel size of 3.75 μm $\times$ 3.75 μm, which leads to a total chip size of 4.8 mm $\times$ 3.6 mm. It has a high quantum efficiency of approximately 37% at 671 nm, which is important for a good signal to noise ratio at short exposure times and low light intensities. This is necessary for later experiments in dipole traps, where the atoms can only scatter with a few photons before they are pushed out of the trap by photon recoils. The minimum exposure time of the camera is 25 μs.

The camera is mounted in front of one of the CF40 viewports which is not used for a MOT beam. In order to decrease the size of the picture by a factor of 3 and focus it on the CCD chip, a telescope consisting of a f = 150 mm lens and a f = 50 lens mounted in a lens tube is used.

Chapter 5

Properties of the MOT

This chapter provides a characterization of our MOT. The loading rate of the MOT was measured for different oven temperatures and the lifetime of atoms in the MOT was determined. All data was taken by fluorescence imaging of the atom cloud.

For an oven temperature of $T_{oven} = 350°$C, the loading rate was determined to be $3 \cdot 10^8$ atoms/s. Since we need approximately $1 \cdot 10^8$ atoms in the MOT to transfer a sufficient number of atoms to the dipole trap, this loading rate is sufficient and will enable fast experiment cycles. Even higher loading rates can be achieved by increasing the oven temperature.

The background pressure limited lifetime of atoms in the MOT was measured to be approximately 23 minutes. This is far longer than the planned experimental cycles and indicates a sufficiently low background collision rate for the planned experiments.

In the first part of this chapter, the imaging method is described. The measured data is presented in the second part.

5.1   Calibration of the imaging system

In order to count the atoms in the MOT, a picture of the fluorescent atom cloud is taken. It is possible to relate the total number of counts on the CCD camera to the atom number by making three assumptions:

- The number of counts on each camera pixel depends linearly on the number of absorbed photons. This is true when the camera is not saturated.

- Photons are emitted in random directions by the atoms and not reabsorbed. This way, the spatial photon distribution is uniform. By measuring the

number of photons emitted into a certain solid angle the total photon number can thus be calculated.

- The scattering rate of photons with an atom is known and constant for a given saturation parameter s_0 and detuning δ_0 of the lasers. For simplicity, full saturation is assumed in our case. This is reasonable since $s_0 \gg 1$ for the MOT beams.

With these requirements fulfilled, the imaging system can be calibrated:

First, the number of photons per count is measured. This is done by shining a laser beam with a known power P and frequency ω onto the CCD sensor of the camera. The total number of counts is extracted from the picture and then compared to the number of photons collected by the chip during the exposure time t_{exp}.

$$N_{photon}^{calib} = \frac{Pt_{exp}}{\hbar\omega} \tag{5.1}$$

$$\eta_{cam} = \frac{N_{photon}^{calib}}{N_{count}^{calib}} \quad . \tag{5.2}$$

Using a 4.5 μW 671 nm laser beam at t_{exp} = 31 μs, we found

$$\eta_{cam}^{671nm} = (1.22 \pm 0.01) \, \frac{\text{photons}}{\text{count}} \quad . \tag{5.3}$$

The error of this value is dominated by the error of the beam power, which is approximately 1%.

Next, the fraction of fluorescence light from the MOT which hits the camera is calculated. Since the imaging system only covers a certain fraction Ω_{cam} of the solid angle, only a fraction of the photons emitted by the atom cloud can be detected. The aperture of the objective has a radius of $r_{aperture}$ = (11.5 $\pm$ 0.5) mm and a distance d_{lens} = (125 $\pm$ 3) mm between the atom cloud and the imaging lens, yielding

$$\Omega_{cam} = \frac{\pi r_{aperture}^2}{4\pi d_{lens}} = (0.0021 \pm 0.0001) \quad . \tag{5.4}$$

As a last step, the photon scattering rate Γ_{sc} per atom is calculated. For resonant light and a saturation parameter $s_0 \gg 1$, the scattering rate of an atom on resonance is

$$\Gamma_{sc} = \frac{\gamma}{2} 2\pi \approx 18\text{MHz} \quad . \tag{5.5}$$

The number of photons scattered by each atom during the exposure time is $N_{sc} = \Gamma_{sc} t_{exp}$.

The number of atoms therefore is

$$N_{atoms}^{res} = \frac{N_{count}\eta_{cam}}{\Omega_{cam}\Gamma_{sc}t_{exp}} \quad . \tag{5.6}$$

For detuned light as used in the MOT, the scattering rate for each atom is lower than in the resonant case. Thus, an additional correction factor κ has to be taken into account. κ is determined experimentally: First, 10 pictures of the atom cloud are taken with the full red-detuning of the MOT (40 MHz). Then, 10 more pictures with the same settings without the red-detuning are taken. This can be done by ramping the MOT beams on resonance right before taking the pictures. Since the MOT requires red-detuning (see 3.2.2) and does not work anymore when the laser is resonant, the pictures have to be taken immediately after ramping.

By dividing the number of counts from the resonant and detuned series of measurement by each other, κ can be found. In our case with a detuning of 40 MHz, it is

$$\kappa = (5.68 \pm 1.59) \quad . \tag{5.7}$$

Equation (5.6) now reads

$$N_{atoms} = \frac{N_{count}\eta_{cam}\kappa}{\Omega_{cam}\Gamma_{sc}t_{exp}} \quad . \tag{5.8}$$

In order to take only counts into account that actually correspond to trapped atoms, it is crucial to subtract the background from each picture.

There are several uncertainties in this calibration method:

- The correction factor κ has a relative error of approximately 28%. This is mainly due to fluctuations of the atom number during calibration.

- The scattering rate is probably slightly lower than assumed since the average MOT beam intensity only leads to an average saturation parameter of $s_0 = 8$. On resonance, this yields a scattering rate of $\Gamma_{sc} = \frac{4}{9}\gamma$ (see chapter 4.3.2). However, the beams are Gaussian and thus the intensity in their middle is higher than average by a factor of 2. This effect should therefore not play a big role for small atom numbers in the MOT, since the atoms then only occupy the middle of the beams. The relative error should be smaller than 10%.

- The error of the solid angle covered by the camera is approximately 5%.

- The error of η_{cam} is approximately 1%.

- Reabsorption of scattered photons is not taken into account.

The relative error of the atom numbers should therefore be on the order of 35%. This is sufficiently low for our measurements of the loading rate and the lifetime of atoms in the trap.

5.2 Experimental data

5.2.1 Loading rate

The loading rate of the MOT was measured for two different oven temperatures, $T_{oven} = 350°$C and $T_{oven} = 400°$C. For each data point, the MOT was loaded for a certain time t_{load}. The Zeeman slower light and field were then turned off and a fluorescence image of the atom cloud was taken. For each loading time, we took a total of 2 - 10 images. The data is shown in figures 5.1 and 5.2.
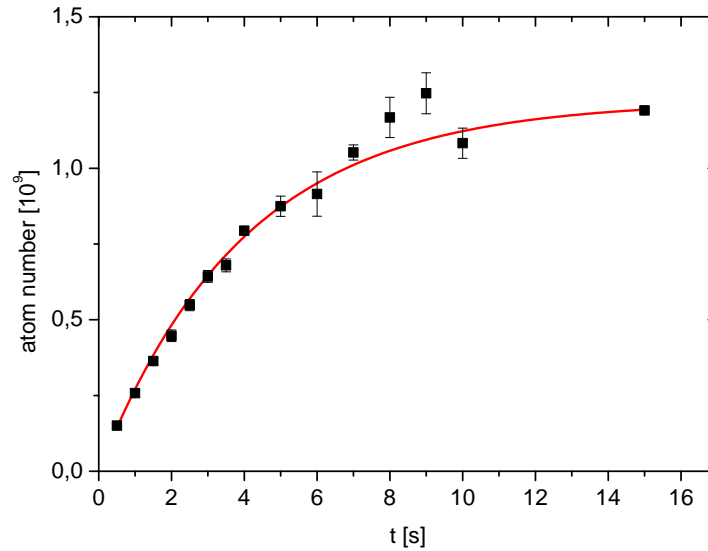

Figure 5.1: Loading curve of the MOT at $T_{oven} = 350°$C. Each data point is the average of 2 - 10 measurements. The error bars represent the standard error of the mean. The loading rate was determined to be L $\approx 3 \cdot 10^8 \frac{\text{atoms}}{\text{s}}$.

When the decay curves of atoms in the MOT were measured (chapter 5.2.2), the low density limit was found to require atom numbers smaller than 10^5 even at a reduced magnetic field gradient. As the atom numbers during the loading process are higher by more than three orders of magnitude even at early stages, it is reasonable to assume that the MOT is density limited. The data was therefore fitted with equation (3.38)

$$N_{load}^{dens-lim}(t) = \frac{L}{R + \beta n_0}(1 - e^{-(R+\beta n_0)t}) \ ,$$

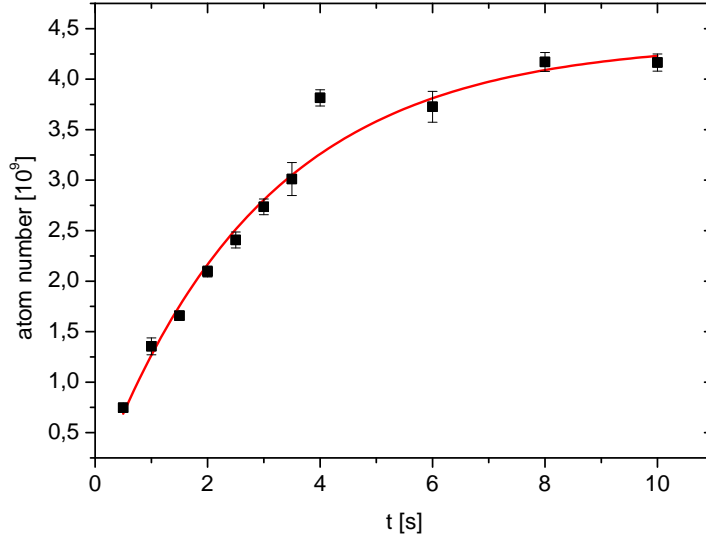which seems to describe the measured curves reasonably well.

Figure 5.2: Loading curve of the MOT at T_{oven} = 400°C. Each data point is the average of 2 - 7 measurements. The error bars represent the standard error of the mean. The loading rate was determined to be L $\approx 1.5 \cdot 10^9 \frac{\mathrm{atoms}}{\mathrm{s}}$.

At an oven temperature of T_{oven} = 350°C, the loading rate obtained from the fit is

$$L = 3 \cdot 10^8 \, \frac{\mathrm{atoms}}{\mathrm{s}} \quad . \tag{5.9}$$

The atom number saturates at

$$N_{max}^{350°} \approx 1.2 \cdot 10^9 \tag{5.10}$$

after approximately 15 seconds.
 For T_{oven} = 400°C, the loading rate obtained from the fit is

$$L = 1.5 \cdot 10^9 \, \frac{\mathrm{atoms}}{\mathrm{s}} \quad . \tag{5.11}$$

The atom number saturates at

$$N_{max}^{400°} \approx 4.4 \cdot 10^9 \tag{5.12}$$

after approximately 10 seconds.
 As discussed above (see chapter 5.1), the relative error of these values is approximately 35%.

Within their errors, our loading rates are slightly higher than those reported for similar oven temperatures from other recent ^{6}Li experiments [Tie09, Sta05].

They are also by a factor of 1.5 higher than the ones measured in our old apparatus ($L \approx 1 \cdot 10^9 \; \frac{\text{atoms}}{\text{s}}$ at $T_{oven} = 400°$C) [Ser07]. This could be due to more laser power in the Zeeman slower. In the old apparatus, the Zeeman slower only provided up to 45 mW, whereas in our setup it has 63 mW. In addition, our Zeeman slower beam and tube have a smaller opening angle ($0.62°$ as compared to $0.95°$). This way, the Zeeman slower beam in our setup can be smaller, which leads to a higher intensity at the same laser power. In a measurement done with the old apparatus, the loading rate was shown to increase with the Zeeman slower beam intensity and not to saturate.

In a typical experiment cycle, we will need approximately $1 \cdot 10^8$ atoms in the MOT, which we will then transfer into an optical dipole trap (see outlook in chapter 6.2). Loading the MOT will therefore be possible in less than one second at an oven temperature of $T_{oven} = 350°$C, which will enable fast experiment cycles and a long oven lifetime.

5.2.2 Lifetime in the trap

As explained in chapter 3.2.2, atoms can escape the trap by two types of processes:

- A *two-body loss process* occurs when two trapped atoms collide with each other. *Two-body losses* dominate the decay curve when the density in the trap is high.

- In a *one-body loss process*, the trapped atom collides with a particle from the background gas. *One-body losses* dominate the lifetime of atoms in the trap when the density in the trap is low.

Two-body losses depend on various experimental parameters such as magnetic field gradient or trapping light intensity and detuning. The planned experiments are not limited by two-body losses from the MOT as they will be done in optical dipole traps. The two-body loss rate therefore is not relevant for them.

The one-body loss rate on the other hand only depends on the vacuum in the experiment chamber. It can therefore be used to characterize the system, serving as a measure for the background pressure. Thus, it is a crucial parameter for the planned experiments in optical dipole traps and optical lattices.

Procedure

In order to measure decay curves, the MOT was loaded with a certain number of atoms. Then, the Zeeman slower was turned off and the atomic beam shutter was closed to prevent further loading and collisions with beam atoms. While the atom cloud was decaying, a series of fluorescence images was taken. The atom number was extracted from each image as described in chapter 5.1.

When the data was taken, there were two constraints for the maximum measurement duration:

- One constraint is heating of the MOT coils. Although they are water cooled, they cannot be driven at the full current for longer than about two minutes. In order to avoid overheating, the current was therefore reduced from 34 A to 20 A. This way, the density of the MOT was decreased, which on the one hand reduced two-body losses, but on the other hand made it easier to reach the low density limit.

- The time during which the atom cloud can be observed in our setup is limited by the FPGAs used in the experiment control system, which use a 32 bit timing address. At a clock speed of 10 MHz, this leads to a maximum experimental cycle duration of approximately 7 minutes. Since the lifetime of atoms in the MOT is on a considerably larger time scale, it is not possible to observe both the two-body and the one-body loss rate in one measurement.

Both constraints are due to the fact that the time scale of the decay is several minutes, whereas the apparatus was designed for experimental cycles of several seconds. They will therefore not affect the performance of the apparatus in the planned experiments.

Two-body loss rate

In order to measure the two-body decay curve, approximately $4 \cdot 10^8$ atoms were loaded into the MOT and their decay was observed. This was done three times. The data can be seen in figure 5.3.

The data cannot be fitted with equation (3.36), which describes the high and low density regimes. On the other hand, the exponential decay expected for the density limited regime (3.39) clearly does not describe the data either. This is probably because the data was taken in a transition regime between the density limited case and the high density case.

A rough order of magnitude estimate of the two-body loss coefficient β can however be obtained with the help of the measured loading curves. Fitting them with equation (3.38) yields $R + \beta n_0 \approx 0.3$. Estimating n_0 from the cloud size and the atom number and neglecting the one-body loss rate R (which is sufficiently
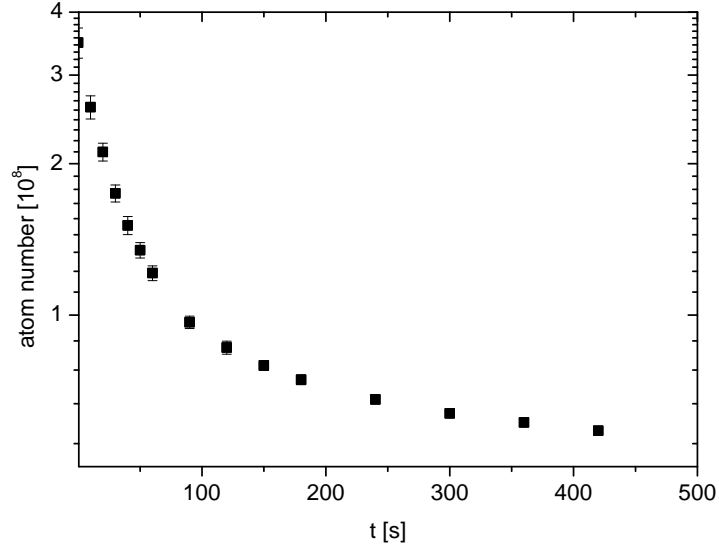
Figure 5.3: Decay curve of the MOT in the two-body loss dominated regime. Each data point is the average of 3 measurements. The error bars represent the standard error of the mean. The vertical axis is logarithmic. A super exponential behavior can easily be seen.

small, see below), β can be found. Assuming a density of approximately 10^{10} atoms/cm^3, this method yields $\beta \approx 3 \cdot 10^{-11}$ cm^3/s. This value matches the ones found in [Kaw93].

One-body loss rate

In order to obtain the one-body loss rate, a low density is needed. This was achieved by reducing the number of atoms to approximately $7 \cdot 10^4$. At higher atom numbers, two-body losses were still dominant and the lifetime could not be determined reliably.

After loading the MOT, a series of pictures of the decaying atom cloud was taken and the atom number was calculated. Figure 5.4 shows the data. The data points were fitted with the exponential decay curve (3.35)

$$N_{decay}^{lo-dens}(t) = N_0 e^{-Rt} \ ,$$

which only takes into account the one-body loss rate R. The lifetime of atoms in the MOT was determined to be

$$\tau = \frac{1}{R} = (1391 \pm 18)s \approx 23\text{min} \ . \tag{5.13}$$
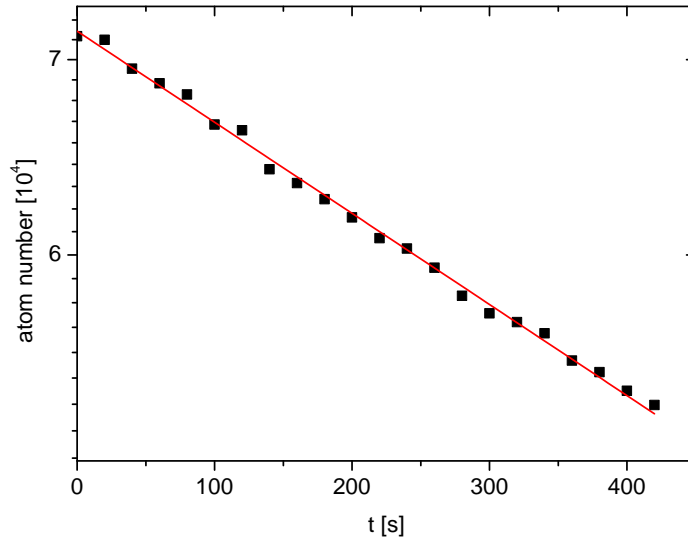
Figure 5.4: Decay curve of the MOT in the one-body loss dominated regime. The vertical axis is logarithmic. The lifetime of atoms in the trap was determined to be $\tau \approx 1391\,\text{s} \approx 23\,\text{min}$.

This timescale is by far longer than any experimental cycle we plan to do with our apparatus. However, for the optical dipole traps we will use, the lifetime will probably be considerably shorter. The dipole potential will be weaker than the MOT, and recapturing processes are very improbable. This should lead to a shorter lifetime.

Still, the long lifetime of atoms in the MOT is an indicator for a sufficiently low background collision rate in the dipole traps. This is especially the case as the value is slightly better than the one measured in our old apparatus [Ser07], where background collisions have never been found to be a limitation.

Chapter 6

Conclusion and Outlook

In the course of this diploma thesis, a vacuum chamber and a magneto-optical trap (MOT) for fermionic ^{6}Li were planned and built. With loading rates of up to $1.5 \cdot 10^9$ atoms/s, the MOT will serve as a first trapping and cooling stage for future experiments with quantum degenerate fermions. It will enable fast experiment cycles as well as a long oven lifetime. The background collision limited lifetime of atoms in the MOT is 23 minutes. We therefore expect that background collisions will not limit the lifetime of atoms in the dipole traps we will use for future experiments.

6.1   Summary

The apparatus consists of a vacuum chamber with a built-in oven, two MOT coils, a Zeeman slower, and a laser system.

 The vacuum chamber is pumped by two titanium sublimation pumps, two ion getter pumps, and a special getter coating in the octagon, which is where atoms are trapped. It is divided into two parts, the experiment chamber and the oven chamber. They are connected by a differential pumping tube. This way, the vacuum in the experiment chamber is not affected by outgassing from the hot oven. The pressure in the experiment chamber is approximately 10^{-11} mbar. In the octagon, it should be considerably lower due to the additional getter coating. In the oven chamber, a pressure of $3 \cdot 10^{-11}$ mbar is reached.

 In order to provide good optical access, the octagon is equipped with six CF40 viewports and two custom made CF100 re-entrant viewports. The re-entrant viewports also provide room for an extra pair of Helmholtz coils, which will enable tuning of the interaction strength between the atoms by means of Feshbach resonances.

 The water cooled MOT coils are mounted directly on the octagon and provide

a magnetic field gradient of $dB/dz \approx 30$ Gauß/cm. The Zeeman slower has a decreasing field configuration so that it can use the MOT field for the last part of the deceleration. This way, the slow atoms are released directly in the MOT and beam expansion after slowing can be reduced. The first part of the Zeeman slower field is provided by eight coils that are wound on the differential pumping tube between the two chambers.

The laser system is built with grating stabilized diode lasers, which are beat locked to the ^{6}Li D2 line with the help of a reference beam.

When the oven is operated at 350°C, it provides enough flux to load approximately 10^8 atoms into the MOT within less than one second. This will enable fast experiment cycles. The lifetime of atoms in the MOT is approximately 23 minutes. This is an indicator for a low background collision rate and thus long lifetimes in the dipole traps we will use for our experiments.

6.2   The next steps

Our experimental goal is to load a gas consisting of atoms in the lowest three ^{6}Li hyperfine components into a two-dimensional optical lattice and to explore its phase diagram. A two-dimensional lattice has the advantages that it is easy to image and that it can be accessed theoretically.
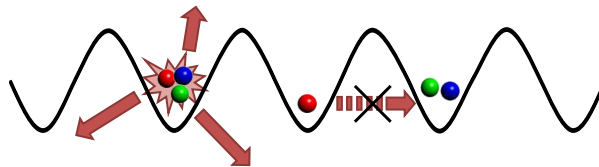

Figure 6.1: Three-body loss blocking in an optical lattice. When three atoms of different spin states meet in one lattice site, they form a trimer and are lost from the trap (left side). The loss can thus serve as a measurement for whether tunneling occurred or not. If the loss rate is much higher than the tunneling rate, the red atom's position is therefore continuously measured (right side). Due to the quantum Zeno effect, tunneling to doubly occupied sites is thus suppressed and the gas is stabilized.

Due to their approximate SU(3) symmetry, three component Fermi gases can be used to model for instance phenomena which occur in quark matter such as color superfluidity and baryon formation [Rap07, Wil07]. However, due to their large three-body loss rate, it is not possible to study their many-body properties in free space. This issue can be overcome by loading them into a periodic potential. When the three-body loss rate γ_3 is higher than the tunneling rate J, the tunneling of an

atom onto a doubly occupied lattice site is suppressed as J^2/γ_3 by the quantum Zeno effect (figure 6.1) [Kan09]. This way, the formation of trimers is prevented and the gas is stabilized.

Another consequence of this three-body constraint is that the ground state of the system is predicted to be a color superfluid phase, where two atoms form Cooper pairs while the third component stays free [Pri10].

6.2.1 Experimental realization

In order to realize such a system, we plan to further cool atoms from the MOT and load them into a two-dimensional optical lattice in three steps. They are illustrated in figure 6.2. First, the atoms are transferred into a large volume optical dipole trap and evaporatively cooled to quantum degeneracy. Next, they are transferred into a pancake-shaped dipole trap. Then, the optical lattice is superimposed with this trap. In a last upgrade, we want to create a lattice with tunable spacing.

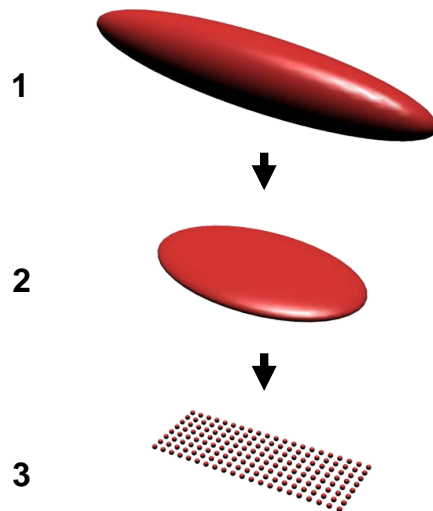In the following, these experimental steps will be reviewed.

Figure 6.2: Planned experimental steps. In step 1, atoms are evaporatively cooled in a large dipole trap. Then, they are transferred into a pancake-shaped dipole trap. In a last step, the lattice potential is superimposed with the pancake trap and a two-dimensional optical lattice is created.

Large dipole trap

First, we plan to load the precooled atoms from the MOT into a large dipole trap. For the dipole trap, we will use a 200W 1064nm Ytterbium fiber laser. By superimposing a beam with its own reflection at an acute angle, a cigar-shaped trap can be created as has been done in our group before [Lom08]. By rotating the polarization of the reflected beam by 90°, interference between the two beams will be prevented.

By applying a homogeneous magnetic field with a pair of Helmholtz coils mounted in the re-entrant viewports, we plan to tune the scattering length via Feshbach resonances. The coils will have 30 windings of 0.5 mm × 7.6 mm capton coated copper wire at an inner radius of 57 mm. They will generate magnetic fields of up to 1500 Gauß at a current of 200 A. The coils will be glued onto water cooled heat sinks similar to those explained in [Zür09].

By tuning the scattering length to large values ($a \approx 3500a_0$), fast thermalization in the trap will be enabled. This way, we should be able to evaporatively cool approximately 10^5 atoms to quantum degeneracy ($T < 200$nK, $T/T_F \approx 0.1$) within a few seconds.

Using the radio frequency (RF) antenna which is built into the vacuum chamber, we will be able to drive transitions between different hyperfine states. This way, we will be able to create a three-component Fermi gas.

Pancake-shaped dipole trap

The next step will be to load the degenerate atoms into a horizontal pancake-shaped optical dipole trap. This trap will be created by crossing two infrared laser beams in a way so that they create an interference pattern of vertically stacked pancakes. The two-dimensional geometry of this trap in combination with high resolution imaging should allow us to do experiments on ferromagnetic domains in a strongly interacting two component Fermi gas.

In order to image atoms in the dipole traps, we will use an objective which was designed in our group and is currently being manufactured. With a numerical aperture of NA = 0.6, it will allow for a resolution of 700 nm over a $\varnothing$ 200 μm field of view. As the objective was optimized for both 671 nm and 1064 nm light, it will also be possible to shine an additional trapping potential into the chamber through the objective.

Optical lattice

In a third step, we want to superimpose the two-dimensional pancake trap with a two-dimensional optical dipole lattice. The lattice will be generated by two perpendicularly superimposed retroreflected infrared (λ = 1064 nm) laser beams.

They will generate a square two-dimensional lattice with a lattice spacing of $d = \lambda/2 = 532$ nm. Figure 6.3 shows the planned optical setup, including the pancake-shaped dipole trap, the lattice, and the objective for high resolution imaging.
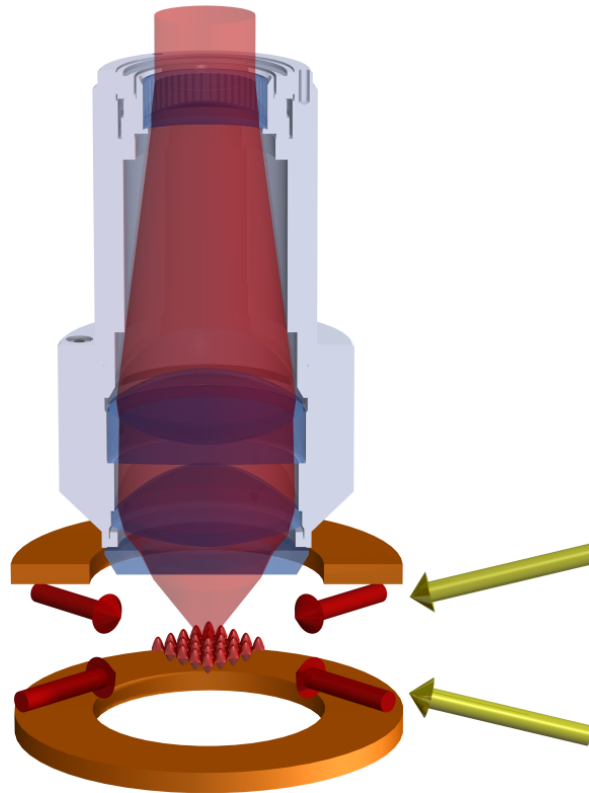

Figure 6.3: Creation of the optical lattice. The yellow beams create the pancake-shaped 2D potential, the red beams create the periodic lattice potential. The Feshbach coils (brown) will allow us to control the interatomic scattering length with the help of Feshbach resonances. The objective will be used for high resolution imaging.

In this lattice, we plan to first do experiments with a two-component Fermi gas. For instance, it should be possible to observe the phase transition between a superfluid and a fermionic Mott insulator. We will then move on to a three-component Fermi gas in the lattice. As a first step, we plan to study the predicted loss blocking mentioned above. Another interesting challenge will be experiments on the atomic color superfluid, which is predicted to exist at low temperatures.

Tunable optical lattice

As an additional upgrade, we plan to generate a tunable optical lattice. This will be done by projecting the lattice potential into the chamber through the objective instead of generating it with horizontal beams. The lattice potential will be created with the help of holographic masks or a spatial light modulator.
 This technique has two main advantages:

- The lattice spacing and geometry can be chosen freely. Single site resolution can be achieved by increasing the lattice spacing.

- The lattice depth can be tuned independently for different areas in the lattice. This way, it should be possible to test lattice cooling schemes which have been proposed in the last years [McK10]. With the help of lattice cooling, it should be possible to reach very low entropies, where phases such as antiferromagnetic ordering are predicted to exist.

Appendix A

Fundamental constants

Symbol	Value	Meaning
$\hbar$	$1.054571628 \cdot 10^{-34}$ Js	Reduced Planck constant
h	$6.62606896 \cdot 10^{-34}$ Js	Planck constant
c	$2.99792458 \cdot 10^{8}$ m/s	Speed of light in vacuum
k_B	$1.3806504 \cdot 10^{-23}$ J/K	Boltzmann constant
a_0	$0.52917720859 \cdot 10^{-10}$ m	Bohr radius
ϵ_0	$8.854187817 \cdot 10^{-12}$ F/m	Vacuum permittivity
μ_B	$927.400915 \cdot 10^{-26}$ J/T	Bohr magneton
m_e	$9.10938215 \cdot 10^{-31}$ kg	Electron mass
M	$9.98834146 \cdot 10^{-27}$ kg	Mass of a ^{6}Li atom
γ_{Li}	$36.898 \cdot 10^{6}$ Hz	Natural linewidth of the ^{6}Li D$_2$ line
λ_{Li}	$670.977338 \cdot 10^{-9}$ m	Wavelength of the ^{6}Li D$_2$ line in vacuum

Table A.1: Constants used in this thesis. The fundamental constants are taken from [NIS], the properties of ^{6}Li can be found in [Geh03].
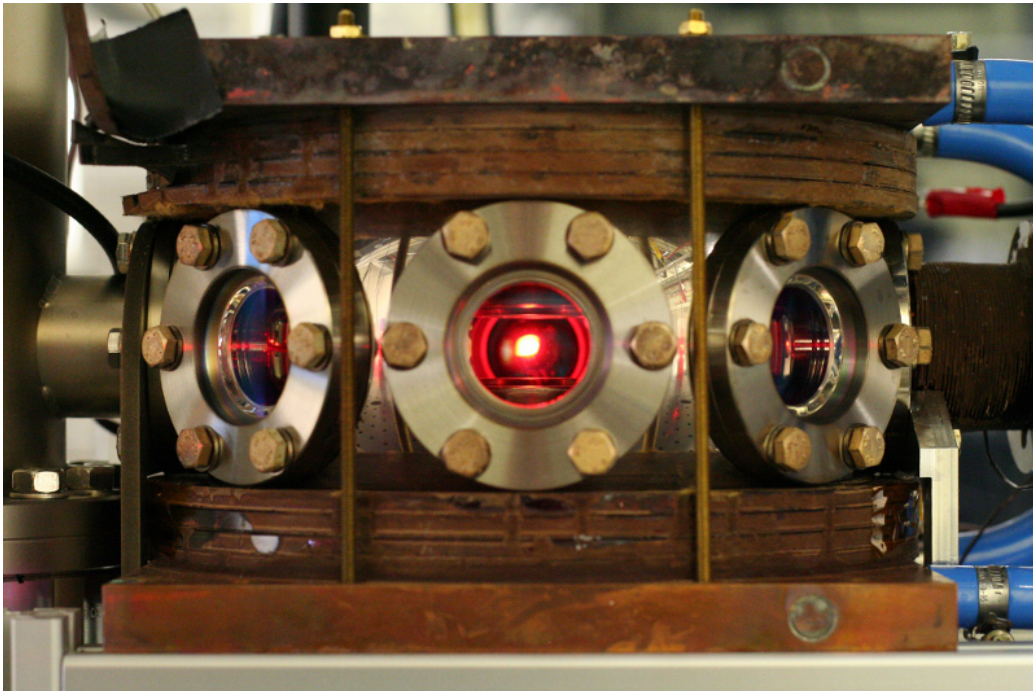
Appendix B

The MOT

Figure B.1: The MOT with approximately $4 \cdot 10^9$ atoms.

Bibliography

[And95]   M. H. Anderson, J. R. Ensher, M. R. Matthews, C. E. Wieman, E. A. Cornell, *Observation of Bose-Einstein condensation in a Dilute Atomic Vapor*, Science **269**, 198--201 (Jul 1995).

[Bak10]   W. S. Bakr, A. Peng, M. E. Tai, R. Ma, J. Simon, J. I. Gillen, S. Folling, L. Pollet, M. Greiner, *Probing the Superfluid-to-Mott Insulator Transition at the Single-Atom Level*, Science **329**(5991), 547--550 (Juli 2010).

[Bar57]   J. Bardeen, L. N. Cooper, J. R. Schrieffer, *Microscopic Theory of Superconductivity*, Phys. Rev. **106**(1), 162--164 (Apr 1957).

[Bar05]   M. Bartenstein, A. Altmeyer, S. Riedl, R. Geursen, S. Jochim, C. Chin, J. H. Denschlag, R. Grimm, A. Simoni, E. Tiesinga, C. J. Williams, P. S. Julienne, *Precise Determination of ^6Li Cold Collision Parameters by Radio-Frequency Spectroscopy on Weakly Bound Molecules*, Phys. Rev. Lett. **94**(10), 103201 (2005).

[Blo05]   I. Bloch, *Ultracold quantum gases in optical lattices*, Nat Phys **1**(1), 23--30 (Oktober 2005).

[Bra08]   E. Braaten, H.-W. Hammer, D. Kang, L. Platter, *Three-body Recombination of Fermionic Atoms with Large Scattering Lengths*, arXiv:cond-mat/arXiv:0811.3578v1 (2008).

[Chi08]   C. Chin, R. Grimm, P. Julienne, E. Tiesinga, *Feshbach Resonances in Ultracold Gases*, Rev. Mod. Phys. **82,**, 1225--1286 (Dezember 2008).

[Dav95]   K. B. Davis, M. O. Mewes, M. R. Andrews, N. J. van Druten, D. S. Durfee, D. M. Kurn, W. Ketterle, *Bose-Einstein condensation in a gas of sodium atoms*, Phys. Rev. Lett. **75**(22), 3969--3973 (Nov 1995).

[DeM99]   B. DeMarco, D. S. Jin, *Onset of Fermi degeneracy in a trapped atomic gas*, Science **285**(5434), 1703--1706 (1999).

[Ein25]   A. Einstein, *Quantentheorie des einatomigen idealen Gases. Zweite Abhandlung*, Sitzungsberichte der preussischen Akademie der Wissenschaften **1** (1925).

[Ess10] T. Esslinger, *Fermi-Hubbard Physics with Atoms in an Optical Lattice*, Annual Review of Condensed Matter Physics **1**(1), 129--152 (2010).

[Geh03] M. E. Gehm, *Properties of* $^6Lithium$ (2003).

[Gra02] S. R. Granade, M. E. Gehm, K. M. O'Hara, J. E. Thomas, *All-Optical Production of a Degenerate Fermi Gas*, Phys. Rev. Lett. **88**(12), 120405 (Mar 2002).

[Gre03] M. Greiner, C. A. Regal, D. S. Jin, *Emergence of a molecular Bose-Einstein condensate from a Fermi gas*, Nature **426**, 537--540 (2003).

[Gri00] Rudolf Grimm, Matthias Weidemüller, Yurii B. Ovchinnikov, *Optical dipole traps for neutral atoms*, Adv. At. Mol. Opt. Phys. **Vol. 42**, 95--170 (2000).

[Hak04] H. Haken, H. C. Wolf, *Atom- und Quantenphysik*, Springer-Lehrbuch ; Physics and astronomy online library (Springer, Berlin ; Heidelberg [u.a.], 2004), 8th Edn.

[Ino98] S. Inouye, M. R. Andrews, J. Stenger, H.-J. Miesner, D. M. Stamper-Kurn, W. Ketterle, *Observation of Feshbach resonances in a Bose-Einstein condensate*, Nature **392**(6672), 151--154 (März 1998).

[Joc03a] S. Jochim, M. Bartenstein, A. Altmeyer, G. Hendl, C. Chin, J. H. Denschlag, R. Grimm, *Pure Gas of Optically Trapped Molecules Created from Fermionic Atoms*, Phys. Rev. Lett. **91**(24), 240402 (Dec 2003).

[Joc03b] S. Jochim, M. Bartenstein, A. Altmeyer, G. Hendl, S. Riedl, C. Chin, J. Hecker Denschlag, R. Grimm, *Bose-Einstein Condensation of Molecules*, Science **302**(5653), 2101--2103 (Dezember 2003).

[Joc09] S. Jochim, *Ultracold Fermi gases: Properties and techniques* (WILEY-VCH, Weinheim, 2009), in: M. Weidemüller, C. Zimmermann (Eds.), Cold Atoms and Molecules, 2nd edition.

[Jul] P. Julienne, *Private Communications, Calculations done according to [Bar05]*.

[Kan09] A. Kantian, M. Dalmonte, S. Diehl, W. Hofstetter, P. Zoller, A. J. Daley, *Atomic Color Superfluid via Three-Body Loss*, Phys. Rev. Lett. **103**(24), 240401-- (Dezember 2009).

[Kaw93] J. Kawanaka, K. Shimizu, H. Takuma, F. Shimizu, *Quadratic collisional loss rate of a* ^7Li *trap*, Phys. Rev. A **48**(2), R883--R885 (Aug 1993).

[Ket08] W. Ketterle, M. W. Zwierlein, *Making, probing and understanding ultracold Fermi gases* (Januar 2008).

[Lom08] T. Lompe, *An apparatus for the production of molecular Bose-Einstein condensates*, Diploma thesis (2008).

[McK10] D. McKay, B. DeMarco, *Cooling in strongly correlated optical lattices: prospects and challenges* (Oktober 2010).

[Met02] H. J. Metcalf, P. v. Straten, *Laser cooling and trapping*, Graduate texts in contemporary physics (Springer, New York ; Berlin ; Heidelberg [u.a.], 2002), corr. 2. print Edn.

[Moe95] A. J. Moerdijk, B. J. Verhaar, A. Axelsson, *Resonances in ultracold collisions of ^6Li, ^7Li, and ^{23}Na*, Phys. Rev. A **51**(6), 4852--4861 (Jun 1995).

[neg] *NEG: Non Evaporable Getter coating: http://est-div-sm.web.cern.ch/est-div-sm/Project-Getter-home.htm.*

[NIS] NIST, *http://physics.nist.gov/cuu/Constants/.*

[Nol06] W. Nolting, *Quantenmechanik - Methoden und Anwendungen* (Springer, Berlin ; Heidelberg [u.a.], 2006), 6th Edn.

[O'H01] K. M. O'Hara, M. E. Gehm, S. R. Granade, J. E. Thomas, *Scaling laws for evaporative cooling in time-dependent optical traps*, Phys. Rev. A **64**(5), 051403 (Oct 2001).

[Ott08] T. B. Ottenstein, T. Lompe, M. Kohnen, A. N. Wenz, S. Jochim, *Collisional Stability of a Three-Component Degenerate Fermi Gas*, Phys. Rev. Lett. **101**(20), 203202 (2008).

[Pri10] A. Privitera, I. Titvinidze, S. Y. Chang, S. Diehl, A. J. Daley, W. Hofstetter, *Loss-induced phase separation and pairing for 3-species atomic lattice fermions* (Oktober 2010).

[Rap07] A. Rapp, G. Zaránd, C. Honerkamp, W. Hofstetter, *Color Superfluidity and ''Baryon'' Formation in Ultracold Fermions*, Phys. Rev. Lett. **98**(16), 160405 (Apr 2007).

[Sch99] U. Schünemann, H. Engler, R. Grimm, M. Weidemüller, M. Zielonkowski, *Simple scheme for tunable frequency offset locking of two lasers*, Rev. Sci. Instrum. **70**(1), 242--243 (Januar 1999).

[Sch05] F. Schwabl, *Quantenmechanik*, Springer-Lehrbuch (Springer, Berlin ; Heidelberg [u.a.], 2005), 6th Edn.

[Ser07] F. Serwane, *The setup of a Magneto Optical Trap for the preparation of a mesoscopic degenerate Fermi gas*, Diploma thesis (2007).

[She10] J. F. Sherson, C. Weitenberg, M. Endres, M. Cheneau, I. Bloch, S. Kuhr, *Single-atom-resolved fluorescence imaging of an atomic Mott insulator*, Nature **467**(7311), 68--72 (September 2010).

[Sim10] P. Simon, *Diploma Thesis* (to be published November 2010).

[Sta05] C. A. Stan, W. Ketterle, *Multiple species atom source for laser-cooling experiments*, Review of Scientific Instruments **76**(6), 063113 (2005).

[Str03] K. E. Strecker, G. B. Partridge, R. G. Hulet, *Conversion of an Atomic Fermi Gas to a Long-Lived Molecular Bose Gas*, Phys. Rev. Lett. **91**(8), 080406 (Aug 2003).

[Tie09] T. G. Tiecke, S. D. Gensemer, A. Ludewig, J. T. M. Walraven, *High-flux two-dimensional magneto-optical-trap source for cold lithium atoms*, Phys. Rev. A **80**(1), 013409 (Jul 2009).

[Wac05] A. Wachter, H. Hoeber, *Repetitorium Theoretische Physik*, Springer-Lehrbuch (Springer-Verlag Berlin Heidelberg, Berlin, Heidelberg, 2005), zweite, überarbeitete auflage Edn., in: Springer-Online.

[Wil07] F. Wilczek, *Quantum chromodynamics: Lifestyles of the small and simple*, Nature Physics **3**, 375--376 (2007).

[Wut00] M. B. Wutz, H. Adam, W. Walcher, K. Jousten (Ed.), *Handbuch Vakuumtechnik* (Vieweg, Braunschweig ; Wiesbaden, 2000), 7th Edn.

[Zür07] G. Zürn, *Assembling a low-cost mechanical laser shutter*, gerhard.zuern@mpi-hd.mpg.de (2007).

[Zür09] G. Zürn, *Realization of an Optical Microtrap for a Highly Degenerate Fermi Gas*, Diploma thesis (2009).

[Zwi03] M. W. Zwierlein, C. A. Stan, C. H. Schunck, S. M. F. Raupach, S. Gupta, Z. Hadzibabic, W. Ketterle, *Observation of Bose-Einstein Condensation of Molecules*, Phys. Rev. Lett. **91**(25), 250401 (Dec 2003).

[Zwi05] M. W. Zwierlein, J. R. Abo-Shaeer, A. Schirotze, C. H. Schunck, W. Ketterle, *Vortices and superfluidity in a strongly interacting Fermi gas*, Nature **435**, 1047--1051 (2005).

Danksagung

Ich möchte mich bei allen bedanken, die zum Gelingen dieser Arbeit beigetragen haben. Insbesondere bedanke ich mich bei:

- Selim, für die hervorragende Betreuung, eine Menge Enthusiasmus und alles, was ich in diesem Jahr von dir gelernt habe.

- dem Ultracold-Team: Timo, Thomas, Friedhelm, Gerhard, André und Phillip für eure Unterstützung und eine tolle Arbeitsatmosphäre. Besonders bedanke ich mich für lange Kicker-Orgien, verrückte Weltverbesserungsideen beim Essen, Versuche zur Schneeball-Ballistik, Stichflammen bis an die Decke, Vakuumkammer kleben, Korrekturlesen bis zum Abwinken, und viel mehr. Jungs, ihr seid die Besten!

- Matthias Weidemüller für die Übernahme des Zweitgutachtens.

- der Gruppe Weidemüller für die gute Zusammenarbeit.

- der Gruppe Ullrich für die gute Atmosphäre und viele Schlachten am Kicker.

- der MPI Werkstatt, insbesondere Florian Säubert und Stephan Flicker von der Lehrwerkstatt, sowie der PI Werkstatt, insbesondere Herrn Ziegler.

- Felix, Jörg, Moritz, Bene, Christian und Felix für unzählige Stunden, die wir über Übungszetteln, Praktikumsversuchen und Büchern gesessen haben. Mit euch hat mein Studium Spaß gemacht!

- meinen Mitbewohnern Kathi, Patrick, Madda und Valentina für einen Platz, wo ich mich wohlfühle.

- meinen Freunden.

- meinen Eltern und Geschwistern. Ohne eure Unterstützung wäre das alles nicht möglich gewesen.

- Monica, für deine Geduld und für's Korrekturlesen. Und für Alles.

Erklärung:

Ich versichere, dass ich diese Arbeit selbstständig verfasst und keine anderen als die angegebenen Quellen und Hilfsmittel benutzt habe.

Heidelberg, den _____   _____
                                                   Unterschrift